Doctoral Thesis

Study on Crystallization Mechanism of Metal-Organic Frameworks(MOFs) by Microfluidic Systems

Yoko Tanaka

Department of Chemistry
Graduate School of Science and Technology
Kwansei Gakuin University

December 2020

Table of Contents

Chapter 1. General introduction

1-1. Metal-Organic Frameworks

1-1-1. Metal-Organic Frameworks

Metal-organic frameworks (MOFs) and porous coordination polymers are three-dimensional infinite complexes composed of metal ions and bridging ligands (Figure 1)[1-2]. Many MOFs have pores of the order of nanometers that are regularly arranged in the structure, making it possible to store and separate gases[3-4]. Taking advantage of these properties, a wide range of research has been conducted on MOFs. The storage and separation of gases such as CO_2 and H_2, which are key to solving environmental problems, have been studied for a long time, and the synthesis of MOFs that show high storage rates or selectivity has been reported[3-6]. In recent years, the activity of metals in pores has been actively studied for catalytic reactions[7-8] and lithium-ion batteries[9-10]. It is known that even in the absence of pores, MOFs exhibit conductivity and carrier transport capacity owing to the high alignment of metals and ligands. In addition, applications in the field of biotechnology, such as drug delivery, are being studied. The properties that can be used in these applications depend greatly on the crystal structure.

MOFs have unlimited structural possibilities with combinations of metal ions and ligands. The selection of metals involves many choices including not only labile metals such as Cu and Zn, but also other inert or high-valence metals such as Zr^{4+}, Cr^{3+} and Ti^{4+} that are difficult to handle. There are many types of ligands, such as common carboxylic acids, pyridines, thiols, and phosphoric acids. Many combinations of metal and ligand have been reported so far. By combining metal ions and ligands, new structures are expected to be created.

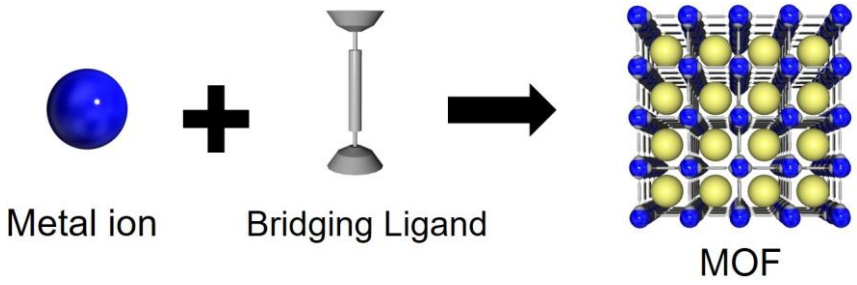

Figure 1. Schematic illustration of Metal-Organic framework

1-1-2. Multicomponent Metal-Organic Frameworks

To increase the MOF structural diversity of MOFs, multicomponent MOFs constructed from more than two types of metal ions or bridging ligands have been actively investigated because they can be designed with high degrees of freedom[11-15]. These are called multicomponent MOFs, whereas MOFs consisting of single type of metal and ligand are called single-linker or single-metal MOFs.

Multicomponent MOFs can be divided into three types (Figure 2). The first type is a multicomponent MOF composed of several kinds of metal ions and a type of ligand[16-17]. For metals with the same valence and similar coordination structures, it is known that mixing two or more of them with one type of ligand yields MOFs that have the same structure as individual metal species. Because the MOFs obtained with this strategy are identical to the known MOF frameworks, there is no need to perform single crystal structure analysis and the time consuming screening process to obtain single crystals. The advantage of this strategy is that the combinations and mixing ratios of metals allow for improved performance and easy tuning of properties.

The second type of multicomponent MOFs consists of multiple ligands with the same basic structure but different substituents[18]. For example, 1,4-benzenedicarboxyate (bdc), a ligand often used in MOF synthesis, has a ligand with various types of substituents. When bdc reacts with Zn, well-known MOF called MOF-5 is produced, but even if multiple ligands with different substituents are mixed, a MOF with the same framework can be obtained. This technique allows for easy addition of functions by substituents.

The third type is multicomponent MOFs composed of completely different ligands and a type of metal source[11, 15]. Only this strategy can create a genuinely new structure. Although this method is the most versatile, it is difficult to control the crystal structures. Therefore, time-consuming screening by trial-and-error is necessary for the discovery of new structures and search for single crystal preparation conditions for structure determination, and powerful tools such as high-throughput methods, are required for screening their synthesis conditions[19-22]. However, it is even more difficult to predict the reaction conditions based on the desired structure, and therefore, it is more challenging to obtain new structures.

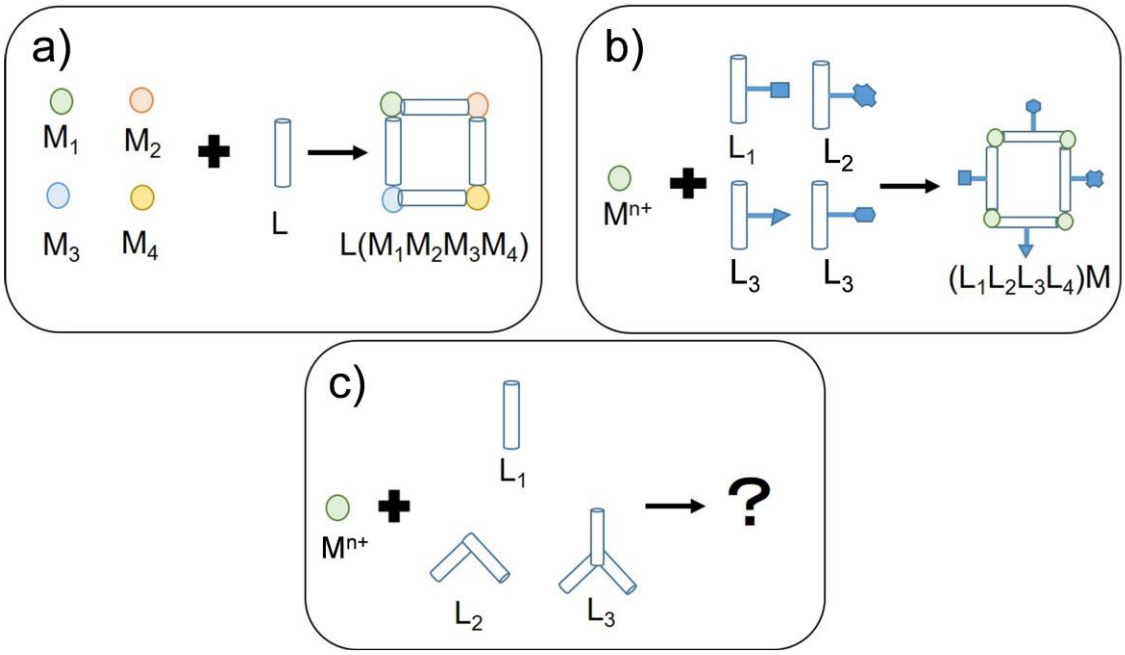

Figure 2. Schematic diagram of three kind of multicomponent MOF; a) MOF composed of different kinds of metal ion and a single type of ligand. b), MOF composed of a single type of metal ion and different types of ligands which has similar structure with different substituent. c) MOF composed of metal ion and various types of ligands.

1-2. Crystallization mechanism of Metal-Organic Frameworks

1-2-1. Classical and non-classical crystallization model

An understanding of the crystallization mechanism is helpful in predicting suitable reaction conditions to synthesize novel MOF structures. Crystallization can generally be divided into two processes: nucleation process and crystal growth process. In the nucleation process, reactants start to react and form a nucleus as a unit in the crystal. This process proceeds quickly. Thereafter, in the crystal growth process, the components of the solution are taken in and the nucleus grows around. This process is called the crystal growth process.

Because the crystal structure is dominated by the nucleation process, control of the nucleation process is important. Especially in the synthesis of MOFs, it is known that crystal polymorphs with different structures can be formed from the same raw material with a small difference in reaction conditions[23-26], thus, the pathway selection by control of the nucleation process is essential. In addition, the balance between the nucleation process and the crystal growth rate influences the size of the crystal which has a significant effect on their properties., therefore the mechanism of this process has received much attention. Therefore, the mechanism of the crystallization process has been actively researched.

As previously reported, crystallization mechanisms can be classified into two types; classical and non-classical model[27] (Figure 3). The classical crystallization model is characterized by processes in which the product is simply generated from the reactant in a single step. In contrast, recently, the non-classical crystallization model is characterized by processes in which intermediates (e.g., clusters or nanoparticles) are generated during crystallization. In both models, an evaluation method to characterize the state during a reaction from multiple perspectives is required.

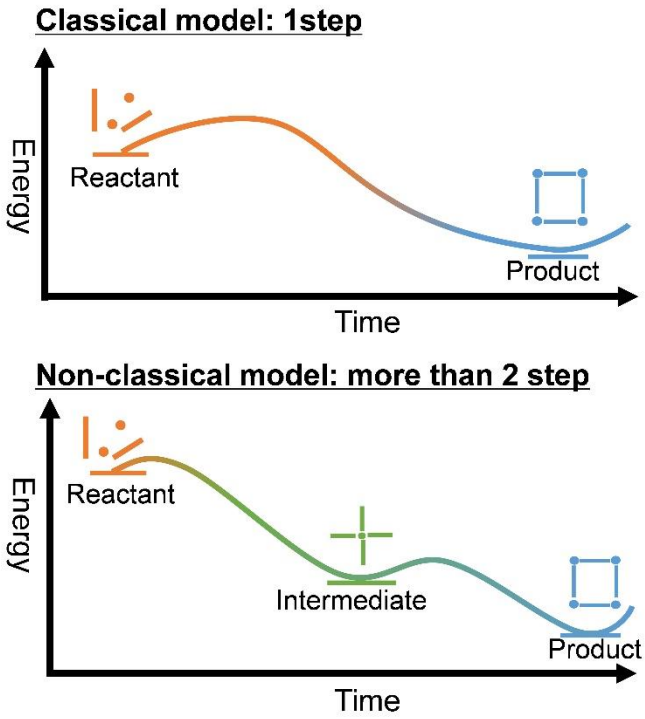

Figure 3. Energy diagram of classical and non-classical model of crystallization.

1-2-2. Reported crystallization mechanism of Metal-Organic Frameworks

The crystallization mechanism of MOFs has been actively studied. It has been reported that several MOFs crystallize by the non-classical mechanism, and a number of in situ techniques have been used to investigate each step of MOF formation in such cases, such as X-ray absorption fine structure (XAFS) spectroscopy[28], nuclear magnetic resonance spectroscopy[29], X-ray diffractometry [30-31], and small/wide-angle X-ray scattering (SAXS/WAXS) techniques[26, 32-33], among others[34-37]. Considerable effort has been made to develop a transparent sealed reaction vessel for use in diffraction and spectroscopy measurements as a measurement cell. However, although in situ experiments using such a sealed reaction vessel allow in situ observation of the reaction mixture in the sample vial, it is difficult to analyze multiple aspects of any state during the reaction process and isolate intermediates. Furthermore, it is difficult to evaluate the state of the nucleation process immediately after the start of the reaction, because such an approach does not result in homogeneity in the batch immediately after the start of the reaction. The crystallization mechanism of multicomponent MOFs is expected to be far more complicated than that of prototypical single-linker MOFs. Therefore, suitable tools for precise reaction control of multicomponent MOFs are needed.

1-3. Microfluidic systems

1-3-1. General usage of microfluidic systems

Continuous fluidic synthesis which is a synthetic method of mixing and reacting a flowing solution in micrometer-order space using microchannel, has attracted much attention[38-48]. Unlike bulk synthesis, mixing within a confined space offers the following advantages. First, continuous mixing in a microspace allows for quick and homogeneous mixing. In large-scale bulk synthesis, internal mixing and temperature inhomogeneities exist due to the heterogeneity caused by agitation and heating. These create non-uniformity in the progress of the reaction within the batch, resulting in the formation of impurities and differences in particle size. In-batch heterogeneity can lead to the formation of impurities and non-uniformity in crystal size, however, these problems can be solved by microfluidic synthesis. In addition, microfluidic channels are thermally efficient and can yield high yields of products in a short time. Therefore, it can be synthesized under milder conditions than bulk synthesis and avoids the risk of explosion caused by handling large quantities of reagents in industrial synthesis. Third, owing to its superiority in handling small quantities of solutions, high-throughput screening can be performed with small amounts of samples. Particularly in the field of biotechnology, "lab-on-a-chip" devices, which allow the synthesis and analysis to be performed in a single micro device, have contributed to the development of this field. Fourth, microfluidics also allows for the selection of different reaction paths than in bulk synthesis by precise control of the mixing process. In flash chemistry of organic synthesis, microfluidic channels allow the selective production of products that cannot be obtained in bulk synthesis by mixing quite quickly. The precise control of the mixing process enables control of the diffusion of substances. This makes it easier to create a far-from-equilibrium state with bulk synthesis. Therefore, it is possible to control the intramolecular interactions of supramolecules to create arbitrary assembly structures. Thus, microfluidic channels are an outstanding vexrsatile device that can be used in a wide range of fields for a variety of purposes.

1-3-2. Usage of micro flow reactor in the field of Metal-Organic Frameworks

Generally, MOFs are synthesized by solvothermal methods under high temperature and pressure; however various methods such as microwave synthesis, electrochemical synthesis, and mechanochemical synthesis have also been developed[49-50]. The advantages and disadvantages of each synthesis method are described below (Table 1).

Table 1. Advantages/disadvantages of synthesis method of MOFs

Synthesis method	Advantages	Disadvantages
Solvothermal synthesis	•General synthesis method and easy for screening of reaction conditions •Suitable for obtaining single crystals	•Dangers of scaling up •Heterogeneity of the reaction in the vessel
Microwave synthesis	•Rapid synthesis •Homogeneity of the reaction in the vessel	•Difficult to control the crystal size as only small crystals can be obtained
Electrochemical synthesis	•Synthesis under milder conditions than hydrothermal synthesis •Film can be prepared in 1step	•Due to limited raw materials, there are few types of MOF to be synthesized. •Single crystals cannot be obtained.
Mechanochemical synthesis	•No organic solvent is needed. •The use of metal oxides as a raw material results in only water as a byproduct	•Difficult to control the crystal size as only small crystals can be obtained

All these methods show difficulty in controlling particle size and scaling. In other words, precise control of the mixing process is difficult in these methods. Microfluidic synthesis can overcome these shortcomings by high thermal efficiency, control of mass diffusion, and precise control of the mixing process (Figure 4). There are three main applications of microchannels in the field of MOFs: 1. efficient synthesis of high-quality MOFs, 2. confined space synthesis of MOF composites with various morphologies, 3. selective synthesis of metastable products.

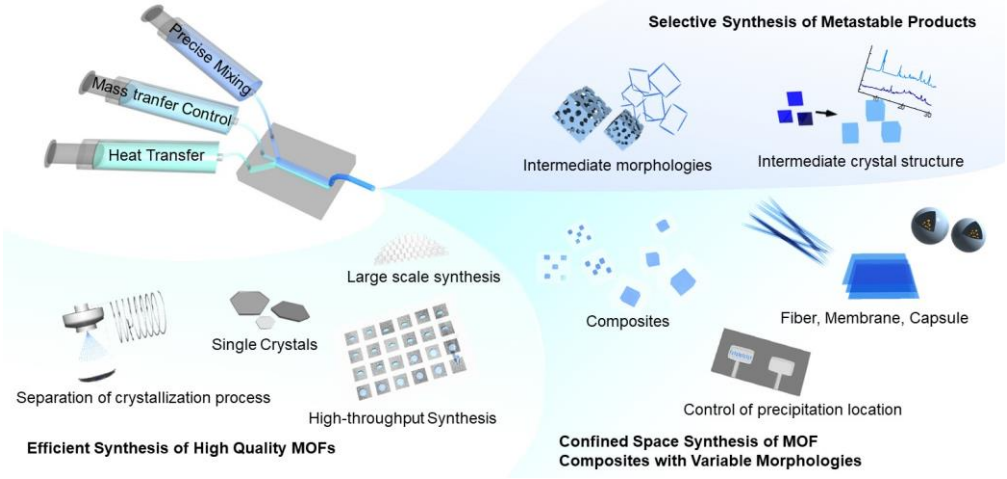

Figure 4. Classification of the previous works of the microfluidics on synthesis of MOFs.

The first application is the efficient synthesis of high-quality MOFs. Microfluidic synthesis allows for quick and homogeneous heating of a solution flowing through a microspace. Therefore, this high heat transfer enables the synthesis in a high yield. In contrast, in conventional bulk synthesis, uneven temperature in the batch causes non-uniform particle size and impurity formation in the batch reaction. In addition, the integration of microfluidic channels allows easy scale-up, which is not dangerous for large-volume synthesis. Therefore, microfluidic MOF synthesis is suitable for large-scale synthesis[50-56]. In addition, in microfluidic synthesis, it is easy to incorporate other operations (e.g. microwave and spray drying), and it is possible to manage any step in the reaction[57-58]. In microfluidic synthesis, the entire process from mixing to crystal deposition takes place within the microfluidic device. The reaction begins in the mixing section of the microfluidic channel, with nucleation occurring slightly behind the mixing section and crystal growth near the exit (i.e., each reaction step corresponds to a specific location). Therefore, the particle size can be easily controlled by accelerating nucleation through manipulations such as irradiating microwaves (MW) to specific locations.In addition, the diffusion of reactants in the microspace can be precisely controlled by adjusting the flow rate of the solution. This technique provides a significant reduction in the diffusion rate and enables the production of high-quality single crystals, which is difficult to achieve with conventional bulk synthesis[59]. Microfluidics is also useful for high-throughput synthesis, as it allows for continuous reactions and precise handling of small amounts of solution. Previous report has reported the synthesis of large numbers of MOF single crystals (up to 6,400 pieces) at a time using a microfluidic device that allowed for control of femtolitre-scale droplets[60].

Second application is confined space synthesis of MOF composites with various morphologies. Although MOF composites, comprising MOFs and other materials, can be produced by stepwise bulk synthesis,[61] this method is poorly suited for precise control of the composite composition and morphology. The exploitation of differences in mixing time and reactivity allows the synthesis of various kinds of composites but is subject to certain limitations. Conversely, microfluidic systems allow precise control over the mixing order of multiple reactants, and thus over composition, which is not possible for bulk synthesis.[62-63]. In microfluidic synthesis, it is possible to continuously produce MOFs with various morphologies, such as fibers, composites, and capsules. These morphologies are formed by the control of mass diffusion. In continuous**,** fluidic synthesis, the reaction space can be controlled by adjusting flow velocity and solvent. For example, in a laminar flow, the reaction proceeds only at the interface of the solution, creating a one-dimensional (1D) reaction field in the direction of the solution flow, which can be used to generate fibers[64]. In

addition, when oil and water layers are mixed, the reaction can only occur at a limited interface, which allows the formation of films and hollow capsules[65-68]. In general, such interfacial reactions are difficult to perform continuously and require additives that may affect the product. In microfluidic synthesis, solution flow can be used to form diverse structures. The use of microfluidic techniques instead of bulk synthesis can afford composites with enhanced performance.

Third application is selective synthesis of metastable products. Microfluidic synthesis allows the precise control of mixing process parameters (e.g., mixing order and timing) that dictate the pathway selection of reaction[69]. As reported in the field of supramolecules[70], by controlling mass diffusion, the field of MOFs has also succeeded in selectively obtaining MOFs of kinetic morphology[71]. Moreover, the reaction time depends on the tube length, which acts as reaction field. Therefore, the observation and isolation of products at any position in the tube at a certain reaction time can be achieved by controlling the flow velocity and concentration[72-73]. Isolation of the solution immediately after mixing allows the characterization of intermediates, such as those produced in the early stages of the reaction. Taken together, the microfluidic channels allow control of the reaction axis and help to selectively obtain non-thermodynamic products. Such products have been reported to exhibit higher adsorption properties than thermodynamic products due to internal defects. Isolation of such metastable kinetic products could be a novel approach to superior material discovery.

1-3-3. Microfluidics on the elucidation of the crystallization mechanism of Metal-Organic Frameworks

To elucidate the crystallization mechanism of multicomponent MOFs, conventional evaluation methods have difficulty evaluating the rapid nucleation process, multifaceted characterization of the intermediate species formed during the reaction, and the individual behavior of the multiple components present during the crystal formation process. The microfluidic system offers the following benefits for the elucidation of the crystallization mechanism and can solve these problems. First, mixing of solutions in microfluidic channels allows for quick and homogeneous mixing. Mixing in bulk creates a heterogeneity in the batch and different progress of the reaction can be observed in different parts of the batch. When observing the crystal formation process, heterogeneity in the batch does not allow us to properly evaluate certain states. In particular, the nucleation process is completed immediately after the start of the reaction, so the system requires homogeneity immediately after the start of mixing. Therefore, microchannel that allow instantaneous mixing of solutions are useful.

Moreover, it allows precise control of the mixing process. In elucidating the crystal formation process of multicomponent MOFs, the influence of each component on the crystal formation process can also be evaluated by precise mixing. The length between the mixing point and an arbitrary endpoint corresponded to the reaction time. These properties facilitate direct observation of dissipative non-equilibrium states by spectroscopy and allow the isolation of reaction intermediates by limiting the reaction time. In addition, the microfluidic channel allows for the stepwise mixing of multiple components and allows for the evaluation of each reactant by controlling the timing and order of the reaction. From these points of view, the use of microfluidics will provide new insights into the crystallization mechanism of multicomponent MOFs.

1-4. Outline of this thesis

The synthesis of novel multicomponent MOFs can expand their structural diversity. However, to obtain new multicomponent MOFs, screening is necessary owing to a lack of guidelines. Therefore, the mechanism of the crystallization process of multicomponent MOFs is investigated to obtain the key to the efficient synthesis of novel multicomponent MOFs. As a tool for elucidating the crystal formation process of multicomponent MOFs, microchannels are considered to be useful based on previous research examples. In this thesis, we report the results of the elucidation of the crystal formation process of multicomponent MOFs by using microchannels to precisely control the non-equilibrium process of crystal formation.

In Chapter 2, we focus on a typical multicomponent MOF, pillared layer MOF CPL-1/2, and investigate the crystal formation process using microchannels. Using microchannel-based synthesis, the effect of flow velocity and ligand mixing order on the nucleation rate was evaluated. Solid-state intermediates were successfully isolated by varying the reaction time. An experimental apparatus was constructed using a combination of microchannels and spectroscopic measurements, and another intermediate in the supersaturated solution immediately after the start of the reaction was determined. Based on these results, we propose a mechanism for the crystal formation of CPL-1/2.

Chapter 3 summarizes this thesis and provides the future outlook.

References

1. Kitagawa, S.; Kitaura, R.; Noro, S., Functional porous coordination polymers. *Angew. Chem. Int. Ed.* **2004,** *43* (18), 2334-2375.

2. Yaghi, O. M.; O'Keeffe, M.; Ockwig, N. W.; Chae, H. K.; Eddaoudi, M.; Kim, J., Reticular synthesis and the design of new materials. *Nature* **2003,** *423* (6941), 705-714.

3. Li, J. R.; Sculley, J.; Zhou, H. C., Metal-organic frameworks for separations. *Chem Rev* **2012,** *112* (2), 869-932.

4. Sumida, K.; Rogow, D. L.; Mason, J. A.; McDonald, T. M.; Bloch, E. D.; Herm, Z. R.; Bae, T. H.; Long, J. R., Carbon dioxide capture in metal-organic frameworks. *Chem Rev* **2012,** *112* (2), 724-81.

5. Li, J.-R.; Kuppler, R. J.; Zhou, H.-C., Selective gas adsorption and separation in metal-organic frameworks. *Chem. Soc. Rev.* **2009,** *38* (5), 1477-1504.

6. Chen, B. L.; Liang, C. D.; Yang, J.; Contreras, D. S.; Clancy, Y. L.; Lobkovsky, E. B.; Yaghi, O. M.; Dai, S., A microporous metal-organic framework for gas-chromatographic separation of alkanes. *Angew. Chem. Int. Ed.* **2006,** *45* (9), 1390-1393.

7. Farrusseng, D.; Aguado, S.; Pinel, C., Metal-Organic Frameworks: Opportunities for Catalysis. *Angew. Chem. Int. Ed.* **2009,** *48* (41), 7502-7513.

8. Lee, J.; Farha, O. K.; Roberts, J.; Scheidt, K. A.; Nguyen, S. T.; Hupp, J. T., Metal-organic framework materials as catalysts. *Chem. Soc. Rev.* **2009,** *38* (5), 1450-1459.

9. Wang, L.; Han, Y.; Feng, X.; Zhou, J.; Qi, P.; Wang, B., Metal–organic frameworks for energy storage: Batteries and supercapacitors. *Coord. Chem. Rev.* **2016,** *307*, 361-381.

10. Xia, W.; Mahmood, A.; Zou, R.; Xu, Q., Metal–organic frameworks and their derived nanostructures for electrochemical energy storage and conversion. *Energ. Environ. Sci.* **2015,** *8* (7), 1837-1866.

11. Bunck, D. N.; Dichtel, W. R., Mixed Linker Strategies for Organic Framework Functionalization. *Chem.-Eur. J.* **2013,** *19* (3), 818-827.

12. Chen, B.; Liang, C.; Yang, J.; Contreras, D. S.; Clancy, Y. L.; Lobkovsky, E. B.; Yaghi, O. M.; Dai, S., A microporous metal-organic framework for gas-chromatographic separation of alkanes. *Angew. Chem. Int. Ed.* **2006,** *45* (9), 1390-3.

13. Deng, H.; Doonan, C. J.; Furukawa, H.; Ferreira, R. B.; Towne, J.; Knobler, C. B.; Wang, B.; Yaghi, O. M., Multiple functional groups of varying ratios in metal-organic frameworks. *Science* **2010,** *327* (5967), 846-50.

14. Lu, W. G.; Wei, Z. W.; Gu, Z. Y.; Liu, T. F.; Park, J.; Tian, J.; Zhang, M. W.; Zhang, Q.; Gentle, T.; Bosch, M.; Zhou, H. C., Tuning the structure and function of metal-organic frameworks via linker design. *Chem. Soc. Rev.* **2014,** *43* (16), 5561-5593.

15. Qin, J. S.; Yuan, S.; Wang, Q.; Alsalme, A.; Zhou, H. C., Mixed-linker strategy for the construction of multifunctional metal-organic frameworks. *J. Mater. Chem. A* **2017,** *5* (9), 4280-4291.

16. Abednatanzi, S.; Gohari Derakhshandeh, P.; Depauw, H.; Coudert, F. X.; Vrielinck, H.; Van Der Voort, P.; Leus, K., Mixed-metal metal-organic frameworks. *Chem Soc Rev* **2019,** *48* (9), 2535-2565.

17. Chen, L.; Wang, H.-F.; Li, C.; Xu, Q., Bimetallic metal–organic frameworks and their derivatives. *Chem. Sci.* **2020,** *11* (21), 5369-5403.

18. Deng, H. X.; Doonan, C. J.; Furukawa, H.; Ferreira, R. B.; Towne, J.; Knobler, C. B.; Wang, B.; Yaghi, O. M., Multiple Functional Groups of Varying Ratios in Metal-Organic Frameworks. *Science* **2010,** *327* (5967), 846-850.

19. Banerjee, R.; Phan, A.; Wang, B.; Knobler, C.; Furukawa, H.; O'Keeffe, M.; Yaghi, O. M., High-throughput synthesis of zeolitic imidazolate frameworks and application to CO2 capture. *Science* **2008,** *319* (5865), 939-943.

20. Biemmi, E.; Christian, S.; Stock, N.; Bein, T., High-throughput screening of synthesis parameters in the formation of the metal-organic frameworks MOF-5 and HKUST-1. *Microporous Mesoporous Mater.* **2009,** *117* (1-2), 111-117.

21. Hertzberg, R. P.; Pope, A. J., High-throughput screening: new technology for the 21st century. *Curr. Opin. Chem. Biol.* **2000,** *4* (4), 445-451.

22. Greeley, J.; Jaramillo, T. F.; Bonde, J.; Chorkendorff, I. B.; Norskov, J. K., Computational high-throughput screening of electrocatalytic materials for hydrogen evolution. *Nat. Mater.* **2006,** *5* (11), 909-913.

23. Karmakar, A.; Paul, A.; Pombeiro, A. J. L., Recent advances on supramolecular isomerism in metal organic frameworks. *CrystEngComm* **2017,** *19* (32), 4666-4695.

24. C. McKinstry, E. J. C., A. J. Fletcher, S. V. Patwardhan, J. Sefcik, Effect of Synthesis Conditions on Formation Pathways of Metal Organic Framework (MOF-5) Crystals. *Cryst. Growth Des.* **2013,** *13* (12), 5481-5486.

25. Gong, X.; Noh, H.; Gianneschi, N. C.; Farha, O. K., Interrogating Kinetic versus Thermodynamic Topologies of Metal-Organic Frameworks via Combined Transmission Electron Microscopy and X-ray Diffraction Analysis. *J. Am. Chem. Soc.* **2019,** *141* (15), 6146-6151.

26. Stavitski, E.; Goesten, M.; Juan-Alcaniz, J.; Martinez-Joaristi, A.; Serra-Crespo, P.; Petukhov, A. V.; Gascon, J.; Kapteijn, F., Kinetic control of metal-organic framework crystallization investigated by time-resolved in situ X-ray scattering. *Angew. Chem. Int. Ed.* **2011,** *50* (41), 9624-8.

27. Van Vleet, M. J.; Weng, T.; Li, X.; Schmidt, J. R., In Situ, Time-Resolved, and Mechanistic Studies of Metal-Organic Framework Nucleation and Growth. *Chem Rev* **2018,** *118*

(7), 3681-3721.

28. Surble, S.; Millange, F.; Serre, C.; Ferey, G.; Walton, R. I., An EXAFS study of the formation of a nanoporous metal-organic framework: evidence for the retention of secondary building units during synthesis. *Chem. Commun.* **2006,** (14), 1518-1520.

29. Haouas, M.; Volkringer, C.; Loiseau, T.; Férey, G.; Taulelle, F., In Situ NMR, Ex Situ XRD and SEM Study of the Hydrothermal Crystallization of Nanoporous Aluminum Trimesates MIL-96, MIL-100, and MIL-110. *Chem. Mater.* **2012,** *24* (13), 2462-2471.

30. Millange, F.; Medina, M. I.; Guillou, N.; Ferey, G.; Golden, K. M.; Walton, R. I., Time-Resolved In Situ Diffraction Study of the Solvothermal Crystallization of Some Prototypical Metal-Organic Frameworks. *Angew. Chem. Int. Ed.* **2010,** *49* (4), 763-766.

31. Yeung, H. H. M.; Wu, Y.; Henke, S.; Cheetham, A. K.; O'Hare, D.; Walton, R. I., InSitu Observation of Successive Crystallizations and Metastable Intermediates in the Formation of Metal-Organic Frameworks. *Angew. Chem. Int. Ed.* **2016,** *55* (6), 2012-2016.

32. Saha, S.; Springer, S.; Schweinefuss, M. E.; Pontoni, D.; Wiebcke, M.; Huber, K., Insight into Fast Nucleation and Growth of Zeolitic Imidazolate Framework-71 by In Situ Time-Resolved Light and X-ray Scattering Experiments. *Cryst. Growth Des.* **2016,** *16* (4), 2002-2010.

33. Cravillon, J.; Nayuk, R.; Springer, S.; Feldhoff, A.; Huber, K.; Wiebcke, M., Controlling Zeolitic Imidazolate Framework Nano- and Microcrystal Formation: Insight into Crystal Growth by Time-Resolved In Situ Static Light Scattering. *Chem. Mater.* **2011,** *23* (8), 2130-2141.

34. Hermes, S.; Witte, T.; Hikov, T.; Zacher, D.; Bahnmuller, S.; Langstein, G.; Huber, K.; Fischer, R. A., Trapping metal-organic framework nanocrystals: An in-situ time-resolved light scattering study on the crystal growth of MOF-5 in solution. *J. Am. Chem. Soc.* **2007,** *129* (17), 5324-+.

35. Jung, S.; Oh, M., Monitoring shape transformation from nanowires to nanocubes and size-controlled formation of coordination polymer particles. *Angew. Chem. Int. Ed.* **2008,** *47* (11), 2049-2051.

36. Goesten, M. G.; de Lange, M. F.; Olivos-Suarez, A. I.; Bavykina, A. V.; Serra-Crespo, P.; Krywka, C.; Bickelhaupt, F. M.; Kapteijn, F.; Gascon, J., Evidence for a chemical clock in oscillatory formation of UiO-66. *Nat. Commun.* **2016,** *7*, 11832.

37. Zheng, C.; Greer, H. F.; Chiang, C.-Y.; Zhou, W., Microstructural study of the formation mechanism of metal–organic framework MOF-5. *CrystEngComm* **2014,** *16* (6), 1064-1070.

38. Sackmann, E. K.; Fulton, A. L.; Beebe, D. J., The present and future role of microfluidics in biomedical research. *Nature* **2014,** *507* (7491), 181-9.

39. Jahnisch, K.; Hessel, V.; Lowe, H.; Baerns, M., Chemistry in microstructured reactors. *Angew. Chem. Int. Ed.* **2004,** *43* (4), 406-46.

40. Psaltis, D.; Quake, S. R.; Yang, C., Developing optofluidic technology through the

fusion of microfluidics and optics. *Nature* **2006,** *442* (7101), 381-6.

41. Song, H.; Chen, D. L.; Ismagilov, R. F., Reactions in droplets in microfluidic channels. *Angew. Chem. Int. Ed.* **2006,** *45* (44), 7336-56.

42. Plutschack, M. B.; Pieber, B.; Gilmore, K.; Seeberger, P. H., The Hitchhiker's Guide to Flow Chemistry. *Chem Rev* **2017,** *117* (18), 11796-11893.

43. Puigmarti-Luis, J., Microfluidic platforms: a mainstream technology for the preparation of crystals. *Chem. Soc. Rev.* **2014,** *43* (7), 2253-2271.

44. Gutmann, B.; Cantillo, D.; Kappe, C. O., Continuous-flow technology-a tool for the safe manufacturing of active pharmaceutical ingredients. *Angew. Chem. Int. Ed.* **2015,** *54* (23), 6688-728.

45. Dittrich, P. S.; Manz, A., Lab-on-a-chip: microfluidics in drug discovery. *Nat Rev Drug Discov* **2006,** *5* (3), 210-8.

46. Shang, L.; Cheng, Y.; Zhao, Y., Emerging Droplet Microfluidics. *Chem Rev* **2017,** *117* (12), 7964-8040.

47. Yoshida, J.; Kim, H.; Nagaki, A., Green and sustainable chemical synthesis using flow microreactors. *ChemSusChem* **2011,** *4* (3), 331-40.

48. Kim, H.; Min, K. I.; Inoue, K.; Im, D. J.; Kim, D. P.; Yoshida, J., Submillisecond organic synthesis: Outpacing Fries rearrangement through microfluidic rapid mixing. *Science* **2016,** *352* (6286), 691-694.

49. Stock, N.; Biswas, S., Synthesis of Metal-Organic Frameworks (MOFs): Routes to Various MOF Topologies, Morphologies, and Composites. *Chem. Rev.* **2012,** *112* (2), 933-969.

50. Rubio-Martinez, M.; Avci-Camur, C.; Thornton, A. W.; Imaz, I.; Maspoch, D.; Hill, M. R., New synthetic routes towards MOF production at scale. *Chem. Soc. Rev.* **2017,** *46* (11), 3453-3480.

51. Dunne, P. W.; Lester, E.; Walton, R. I., Towards scalable and controlled synthesis of metal–organic framework materials using continuous flow reactors. *React. Chem. Eng.* **2016,** *1* (4), 352-360.

52. Rubio-Martinez, M.; Batten, M. P.; Polyzos, A.; Carey, K. C.; Mardel, J. I.; Lim, K. S.; Hill, M. R., Versatile, High Quality and Scalable Continuous Flow Production of Metal-Organic Frameworks. *Sci. Rep.* **2014,** *4*.

53. Didriksen, T.; Spjelkavik, A. I.; Blom, R., Continuous synthesis of the metal—organic framework CPO-27-Ni from aqueous solutions. *J. Flow Chem.* **2017,** *7* (1), 13-17.

54. Gimeno-Fabra, M.; Munn, A. S.; Stevens, L. A.; Drage, T. C.; Grant, D. M.; Kashtiban, R. J.; Sloan, J.; Lester, E.; Walton, R. I., Instant MOFs: continuous synthesis of metal-organic frameworks by rapid solvent mixing. *Chem. Commun.* **2012,** *48* (86), 10642-4.

55. Jambovane, S. R.; Nune, S. K.; Kelly, R. T.; McGrail, B. P.; Wang, Z.; Nandasiri, M. I.;

Katipamula, S.; Trader, C.; Schaef, H. T., Continuous, One-pot Synthesis and Post-Synthetic Modification of NanoMOFs Using Droplet Nanoreactors. *Sci Rep* **2016,** *6*, 36657.

56. Schoenecker, P. M.; Belancik, G. A.; Grabicka, B. E.; Walton, K. S., Kinetics study and crystallization process design for scale-up of UiO-66-NH2synthesis. *AIChE J.* **2013,** *59* (4), 1255-1262.

57. Albuquerque, G. H.; Fitzmorris, R. C.; Ahmadi, M.; Wannenmacher, N.; Thallapally, P. K.; McGrail, B. P.; Herman, G. S., Gas–liquid segmented flow microwave-assisted synthesis of MOF-74(Ni) under moderate pressures. *CrystEngComm* **2015,** *17* (29), 5502-5510.

58. Garzón-Tovar, L.; Cano-Sarabia, M.; Carné-Sánchez, A.; Carbonell, C.; Imaz, I.; Maspoch, D., A spray-drying continuous-flow method for simultaneous synthesis and shaping of microspherical high nuclearity MOF beads. *React. Chem. Eng.* **2016,** *1* (5), 533-539.

59. Sorrenti, A.; Jones, L.; Sevim, S.; Cao, X.; deMello, A. J.; Marti-Gastaldo, C.; Puigmarti-Luis, J., Growing and Shaping Metal-Organic Framework Single Crystals at the Millimeter Scale. *J. Am. Chem. Soc.* **2020,** *142* (20), 9372-9381.

60. Witters, D.; Vergauwe, N.; Ameloot, R.; Vermeir, S.; De Vos, D.; Puers, R.; Sels, B.; Lammertyn, J., Digital microfluidic high-throughput printing of single metal-organic framework crystals. *Adv. Mater.* **2012,** *24* (10), 1316-20.

61. Zhu, Q. L.; Xu, Q., Metal-organic framework composites. *Chem Soc Rev* **2014,** *43* (16), 5468-512.

62. Hu, C.; Bai, Y. X.; Hou, M.; Wang, Y. S.; Wang, L. C.; Cao, X.; Chan, C.; Sun, H.; Li, W. B.; Ge, J.; Ren, K. N., Defect-induced activity enhancement of enzyme-encapsulated metal-organic frameworks revealed in microfluidic gradient mixing synthesis. *Sci. Adv.* **2020,** *6* (5), eaax5785.

63. Faustini, M.; Kim, J.; Jeong, G. Y.; Kim, J. Y.; Moon, H. R.; Ahn, W. S.; Kim, D. P., Microfluidic Approach toward Continuous and Ultrafast Synthesis of Metal-Organic Framework Crystals and Hetero Structures in Confined Microdroplets. *J. Am. Chem. Soc.* **2013,** *135* (39), 14619-14626.

64. Puigmarti-Luis, J.; Rubio-Martinez, M.; Hartfelder, U.; Imaz, I.; Maspoch, D.; Dittrich, P. S., Coordination polymer nanofibers generated by microfluidic synthesis. *J. Am. Chem. Soc.* **2011,** *133* (12), 4216-9.

65. Brown, A. J.; Brunelli, N. A.; Eum, K.; Rashidi, F.; Johnson, J. R.; Koros, W. J.; Jones, C. W.; Nair, S., Interfacial microfluidic processing of metal-organic framework hollow fiber membranes. *Science* **2014,** *345* (6192), 72-75.

66. Eum, K.; Rownaghi, A.; Choi, D.; Bhave, R. R.; Jones, C. W.; Nair, S., Fluidic Processing of High-Performance ZIF-8 Membranes on Polymeric Hollow Fibers: Mechanistic Insights and Microstructure Control. *Adv. Funct.* **2016,** *26* (28), 5011-5018.

67. Ameloot, R.; Vermoortele, F.; Vanhove, W.; Roeffaers, M. B. J.; Sels, B. F.; De Vos, D. E., Interfacial synthesis of hollow metal-organic framework capsules demonstrating selective permeability. *Nat. Chem.* **2011,** *3* (5), 382-387.

68. Jeong, G.-Y.; Ricco, R.; Liang, K.; Ludwig, J.; Kim, J.-O.; Falcaro, P.; Kim, D.-P., Bioactive MIL-88A Framework Hollow Spheres via Interfacial Reaction In-Droplet Microfluidics for Enzyme and Nanoparticle Encapsulation. *Chem. Mater.* **2015,** *27* (23), 7903-7909.

69. Sorrenti, A.; Leira-Iglesias, J.; Markvoort, A. J.; de Greef, T. F. A.; Hermans, T. M., Non-equilibrium supramolecular polymerization. *Chem Soc Rev* **2017,** *46* (18), 5476-5490.

70. Numata, M., Supramolecular Chemistry in Microflow Fields: Toward a New Material World of Precise Kinetic Control. *Chem Asian J* **2015,** *10* (12), 2574-88.

71. Rubio-Martinez, M.; Imaz, I.; Domingo, N.; Abrishamkar, A.; Mayor, T. S.; Rossi, R. M.; Carbonell, C.; deMello, A. J.; Amabilino, D. B.; Maspoch, D.; Puigmarti-Luis, J., Freezing the Nonclassical Crystal Growth of a Coordination Polymer Using Controlled Dynamic Gradients. *Adv. Funct.* **2016,** *28* (37), 8150-8155.

72. Wang, Y.; Li, L.; Dai, P.; Yan, L.; Cao, L.; Gu, X.; Zhao, X., Missing-node directed synthesis of hierarchical pores on a zirconium metal–organic framework with tunable porosity and enhanced surface acidity via a microdroplet flow reaction. *J. Mater. Chem. A* **2017,** *5* (42), 22372-22379.

73. Wang, Y.; Li, L.; Liang, H.; Xing, Y.; Yan, L.; Dai, P.; Gu, X.; Zhao, G.; Zhao, X., Superstructure of a Metal-Organic Framework Derived from Microdroplet Flow Reaction: An Intermediate State of Crystallization by Particle Attachment. *ACS Nano* **2019,** *13* (3), 2901-2912.

Chapter 2

Elucidation of crystallization mechanism of CPL-1/2 by microfluidic systems

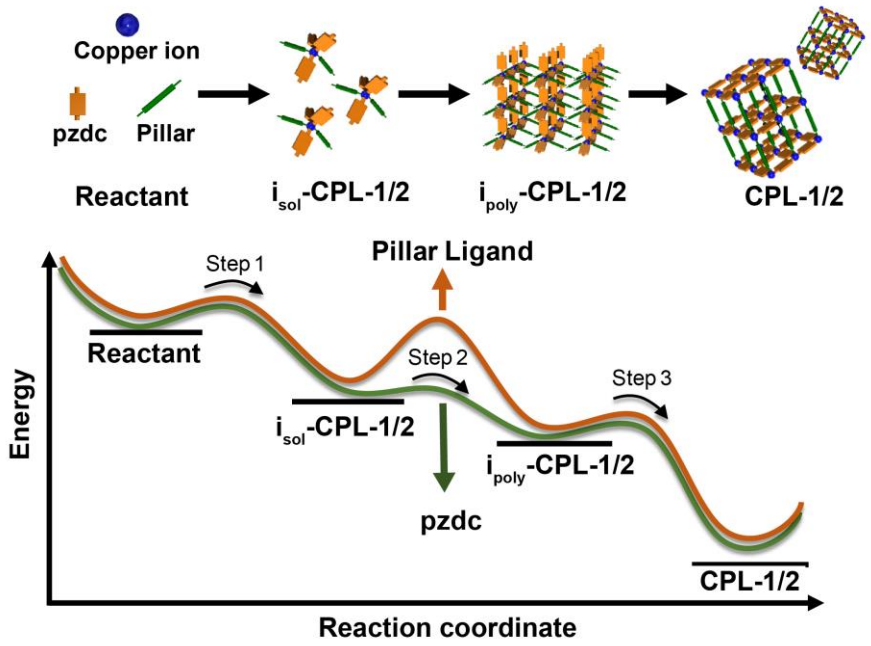

Abstract: To diversify metal-organic frameworks (MOFs), multi-component MOFs constructed from more than two kinds of bridging ligand have been actively investigated due to the high degree of design freedom afforded by the combination of multiple ligands. Predicting the synthesis conditions for such MOFs requires an understanding of the crystallization mechanism, which has so far remained elusive. In this context, microflow systems are efficient tools for capturing non-equilibrium states as they facilitate precise and efficient mixing with reaction times that correspond to the distance from the mixing point, thus enabling reliable control of non-equilibrium crystallization processes. Herein, one of the representative multi-component MOF CPL-1/2 with pillared-layer structure was synthesized by microfluidic synthesis and the intermediates were observed by an in situ measurement system that combines microflow reaction with UV-Vis and X-ray absorption fine structure spectroscopies, thereby enabling their rapid nucleation to be monitored. Based on the results, a three-step nonclassical nucleation mechanism involving two kinds of intermediate is proposed.

2-1. Introduction

Understanding of the crystal formation mechanism of multicomponent MOFs is helpful in the investigation of novel MOFs because the reaction conditions are difficult to predict.
Although there are various types of multicomponent MOFs, the pillared layer type is a good model for this study. The “pillared-layer strategy” is a conventional synthesis approach that overcomes the difficulties in predicting the structures of multi-component MOFs[74-78] (Figure 1). In a typical pillared-layer motif, metal ions and anionic organic ligands, such as carboxylates, form neutral two-dimensional (2D) structures, and these 2D sheets are connected through neutral “pillar” ligands that are typically heteroaromatic amines. This design strategy is well established, and a large number of MOFs, containing both layer ligands and pillar ligands have been reported. This technique allows for easy adjustment of pore size by varying the length of different pillar ligands while maintaining the same layered structure. Therefore, pillared-layer MOFs have been used in many studies. To elucidate the mechanism of crystal formation, the pillared-layered MOFs were considered to be suitable due to their simple structure and ease of synthesis.

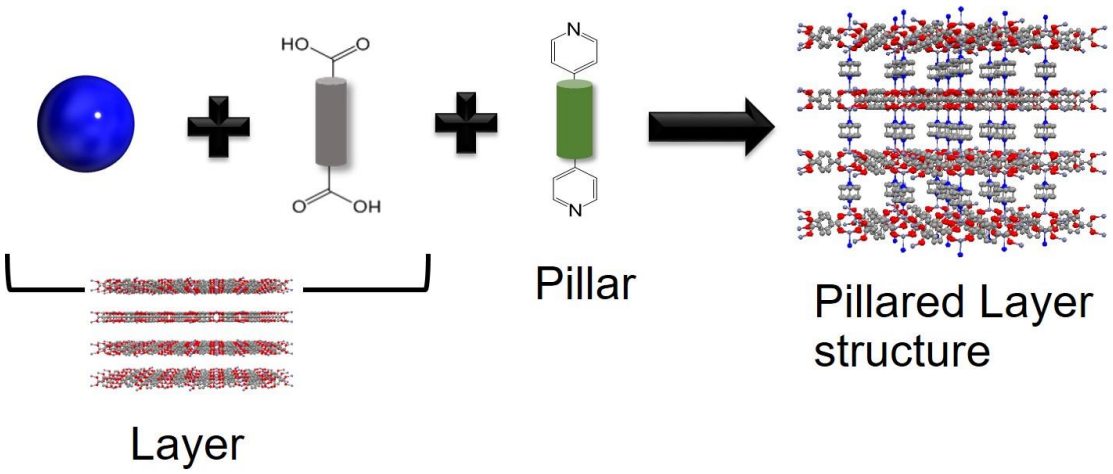

Figure 1. Schematic illustration of pillared layer MOFs

However, even the crystallization mechanisms of pillared-layer MOFs are not well understood. Although X-ray diffraction data have been collected during the syntheses of pillared-layer MOFs[31], the role of each ligand in the crystallization process has not been independently determined due to complex competition between the two coordinating ligands in the reaction solution. A deeper understanding of the crystallization mechanisms of pillared-layer MOFs could therefore provide a reasonable general

starting model for elucidating and controlling the self-assembly of multi-component MOFs.

As such, the use of microfluidics is a valuable approach for elucidating the complex crystallization processes of MOFs. This approach offers the following benefits. First, in-microchannel synthesis has a high rmixing efficiency than bulk synthesis, which results in reduced reaction time and higher efficiency. Second, the small microchannel dimensions allow the precise control of substance diffusion. Third, the microreactors can modify the reaction axis via slight adjustments to the reaction conditions. In particular, the reaction pathway is sensitive to mixing time differences of several microseconds

An understanding of the non-equilibrium crystal-forming processes of multi-component MOFs and control over their crystal polymorphism would therefore be expected to radically facilitate rational design of the crystal structures and/or morphologies of multi-component MOFs.

In this work, CPL-1/2, a pillared-layer MOF, was focused on to elucidate the crystal formation process. In particular, the influence of precise mixing of multiple components on crystallization, an important aspect in the synthesis of multicomponent MOFs, is discussed. In particular, the influence of precise mixing of multicomponents on crystallization is discussed. In this chapter, experiments of bulk and microfluidic synthesis (2-2-1, 2) and spectroscopic measurements using UV-vis and X-ray absorption measurements (2-2-3) are presented to propose a mechanism of crystal formation (2-2-4).

2-2. Result and Discussion

2-2-1. Synthesis of CPL-1/2 by bulk synthesis

In this study, we focused on CPL-1/2, one of the representative pillared-layer MOFs (Figure 2a)[79]. Both structures have been widely studied over the years[80-83], especially CPL-1 for the separation of acetylene[77] and CPL-2 for the study of the shape-responsive transformation caught the attention. CPL-1/2 have pillared-layer structures that consist of layers composed of Cu(II), pzdc (Figures 2b), and either pyz or bpy as pillar ligands, respectively (Figure 2b). Three carboxylate oxygen atoms, one nitrogen atom of the pzdc unit, and one nitrogen atom of a pyrazine unit form a distorted square-pyramidal coordination geometry around the Cu(II) ion (Figure 2c and 2d). While MOFs are generally required to be synthesized at high temperature and pressure, CPL-1/2 are synthesized in water and/or methanol at ambient temperature

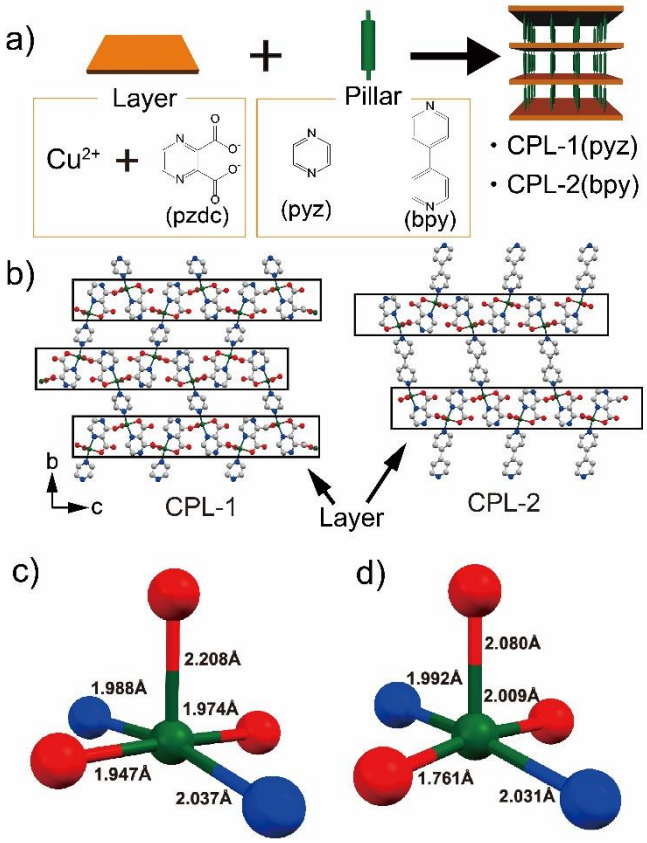

Figure 2. a) Schematic representation of the pillared-layer structures of CPL-1 and CPL-2. b) The crystal structures of CPL-1/2 along the a axis; C gray, O red, N blue, and Cu green. H atoms are omitted for clarity. The local structures of (c) CPL-1, and (d) CPL-2. C gray, O red, N blue, Cu green. H atoms are omitted for clarity.

We synthesized CPL-1/2 in accordance with the reported bulk synthesis method through the reaction of $Cu(ClO_4)_2 \cdot 6H_2O$, sodium 2,3-pyrazinedicarboxylate (Na_2pzdc), and bridging pillar ligands (pyz or bpy). CPL-1 was prepared using 12 equivalents of pyz, while CPL-2 was prepared using 0.6 equivalents of bpy relative to $Cu(ClO_4)_2 \cdot 6H_2O$. The mixed CPL-1 solution remained transparent for several minutes, after which time crystals began to precipitate (Figure 3). In contrast, the CPL-2 solution rapidly became turbid during mixing. The prepared crystals were characterized by and scanning electron microscopy (SEM) (Figures 3c and 3d) X-ray powder diffractometry (XRPD) (Figure 5). SEM images shows that CPL-1 crystals were ~10 μm in size, on average, while those of CPL-2 were ~100 nm in size.

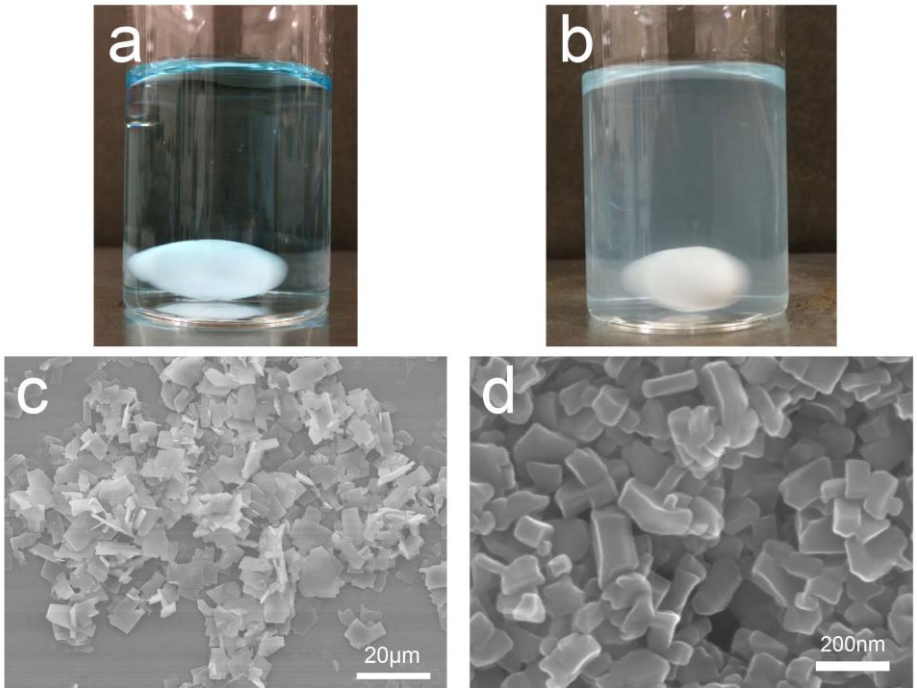

Figure 3. Reaction solutions after mixing for 20 s: a) CPL-1, and b) CPL-2. The reaction solution of CPL-1 was transparent in its supersaturated state. In contrast, that of CPL-2 was cloudy, which is indicative of the commencement of crystal precipitation. This difference indicates that the nucleation rate of CPL-1 was slower than that of CPL-2. SEM images of c) CPL-1, and d) CPL-2 synthesized by the bulk synthesis route.

Generally, crystallization can be divided into two main processes, namely nucleation and crystal growth. The crystal size was determined by the valance of the nucleation rate and crystal growth rate (Figure 4). Fast nucleation results in a high nucleus concentration

that produces small particles, while slow nucleation results in a low concentration of initial seeds that consume larger amounts of precursor per nucleus, resulting in larger particles. According to this mechanism, the crystal size tends to reflect the balance between the rates of nucleation and crystal growth. When the nucleation is fast and occurs within the initial period, a large number of nuclei are generated rapidly, and slow growth results in the formation of small crystals. Observation of the reaction solutions and crystal sizes revealed that CPL-1 nucleates more slowly than CPL-2, thereby suggesting that the nucleation process may be suppressed by excess amounts of pyz (12 eq. for CPL-1) or be enhanced by bpy (0.6 eq. for CPL-2).

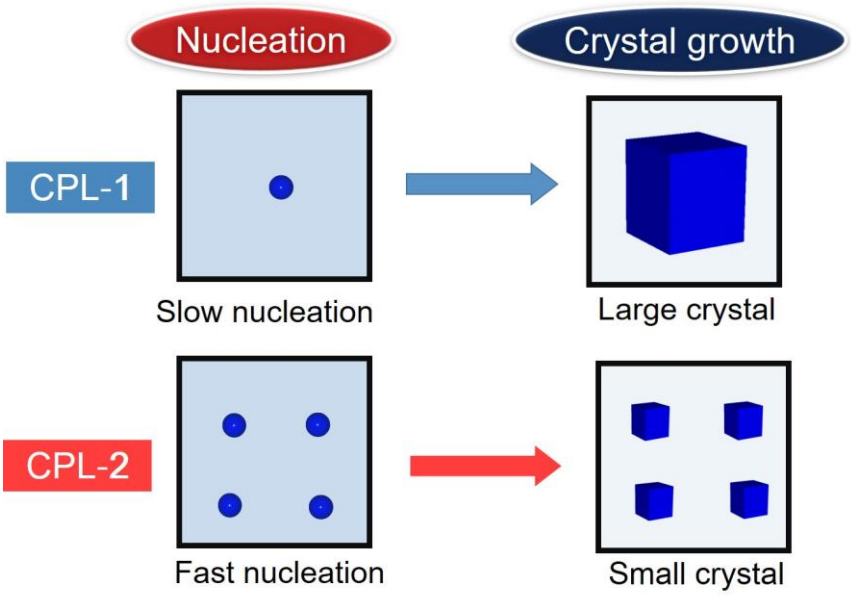

Figure 4. Effect on the crystal size by the difference of nucleation rate

The resulting crystals were confirmed as CPL-1 and 2 by XRPD measurements (Figure 5b, d).

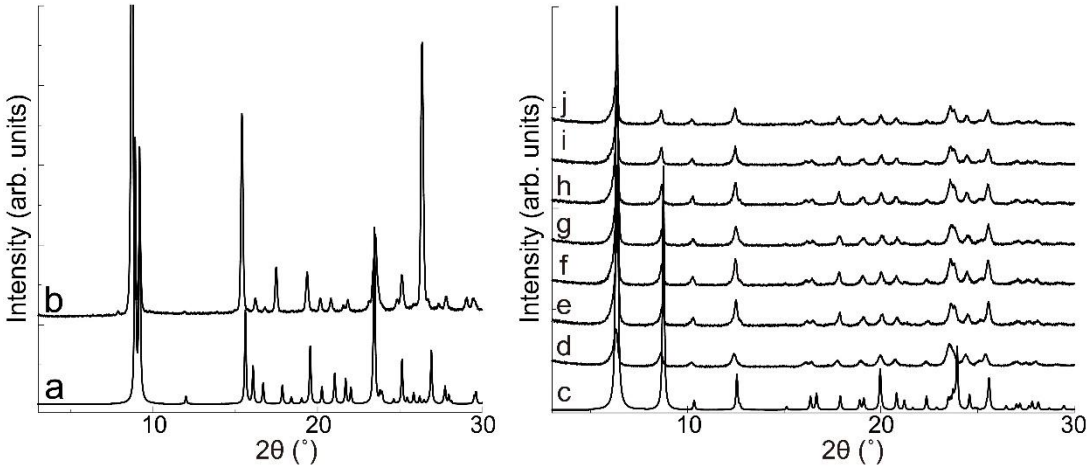

Figure 5. XRPD patterns of CPL-1 and CPL-2 prepared by the bulk and fluidic synthesis routes. **Left**: (a) The simulated diffraction pattern of CPL-1, and (b) the XRPD pattern of CPL-1 crystals prepared by the bulk synthesis route. **Right**: (c) Simulated diffraction pattern of CPL-2, and the XRPD patterns of CPL-2 crystals prepared by (d) the bulk and fluidic synthesis routes at flow rates of: e) 0.5, (f) 1, (g) 3, (h) 5, (i) 7, and (j) 10 mL/min, with 2.5 mM $Cu(ClO_4)_2 \cdot 6H_2O$. The spectra of all obtained crystals, including those not shown in this figure, are consistent with that simulated for CPL-2, which indicates that the synthesis method employed does not influence the structure.

To obtain an understanding of the factors that determine the nucleation rate, we synthesized CPL-2 using various amounts of the pillar ligand, where larger amounts of 4,4'-bpy or pyridine (i.e., a monodentate heteroaromatic ligand) as a modulator led to larger CPL-2 crystal. In the synthesis of MOF, additives called modulators are added besides the reactants to control the particle size, such as to obtain single crystals or to obtain nanometer size[84]. Typically, a monodentate ligand is added to the reaction because of competition with a bridging ligand to affect the rate of crystal formation. In this case, we added a pyridine, which may compete with 4,4'-bpy, to evaluate the effect; SEM images of crystals synthesized with large amounts of 4,4'-bpy and pyridine show that the addition of the piller ligand or the modulator would have a greater effect on the grain size to be larger (Figure 6). This result suggests that the nitrogen-based pillar ligands play key roles in suppressing nucleation processes; the copper ion and the pillar ligand can form stable coordination compounds in solution, which prevents the formation of the nucleus.

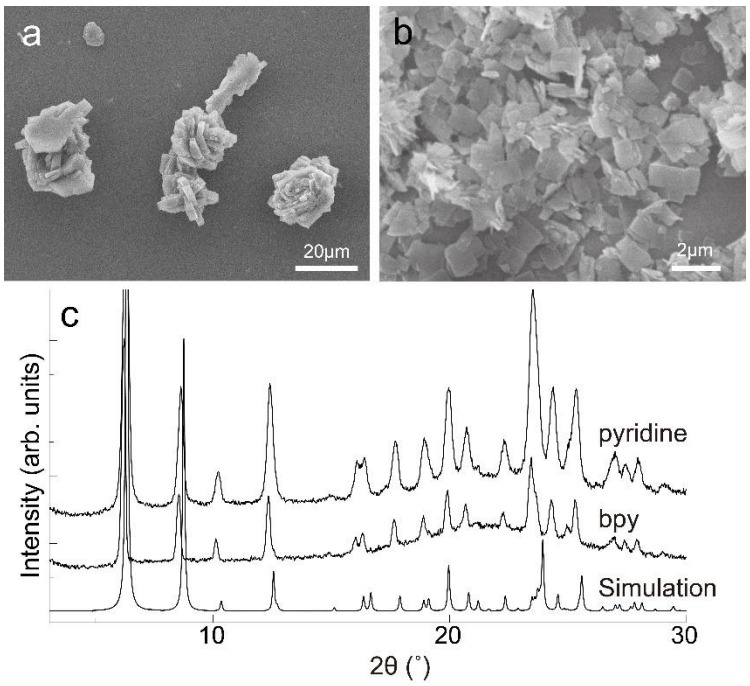

Figure 6. SEM images of CPL-2 crystals synthesized with excess amounts of a) bpy (12 eq.), and b) pyridine (8 eq.). c) XRPD patterns of crystals of a) and b).

2-2-2. Fluidic synthesis of CPL-1/2

The fluidic synthesis route using an acrylic Y-shaped microflow reactor (with a 40° confluence angle) as shown in Figure 7 was carried out. The solution compositions were the same as those used in the reported bulk synthesis. CPL-1 was prepared using 12 equivalents of pyz, while CPL-2 was prepared using 0.6 equivalents of bpy relative to $Cu(ClO_4)_2 \cdot 6H_2O$. All-plastic disposable syringes were filled with a mixed aqueous solution (10 mL) of $Cu(ClO_4)_2 \cdot 6H_2O$ (1.3–20 mM) and pyz (16.1–248 mM), and were filled with 10 mL sodium 2,3-pyrazinedicarboxylic acid aqueous solution (1.3–20 mM) for CPL-1. For CPL-2, an aqueous solution of $Cu(ClO_4)_2 \cdot 6H_2O$ (1.3–20 mM, 10 mL) and a solution of sodium 2,3-pyrazinedicarboxylic acid (1.3–20 mM) and 4,4'-bipyridine (0.8–12 mM) in 1:1 methanol:water (10 mL). The solutions were pumped into the reactor through 1-mm-diameter tubes by two syringe pumps. The mixed solution was allowed to stand for ~12 h, after which the precipitate was separated by centrifugation or filtration (depending on the particle size) and washed twice with methanol. The crystals obtained in this manner were characterized by XRPD, and SEM. The SEM images reveal that the crystals are strongly condensed, making it difficult to distinguish a single crystallite. Therefore, we considered an aggregated particle to be one crystalline particle and compared the sizes of the crystalline particles in their aggregated states.

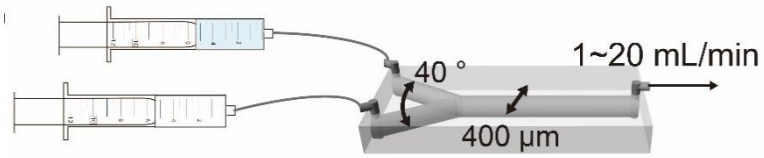

Figure 7. Schematic diagram of one step fluidic synthesis

The flow synthesis of CPL-1 was carried out at different velocities, and the SEM images showed that the crystal size did not changed even at different velocities (Figure 8). The flow velocity did not affect the crystal size in different concentrations of CPL-1.

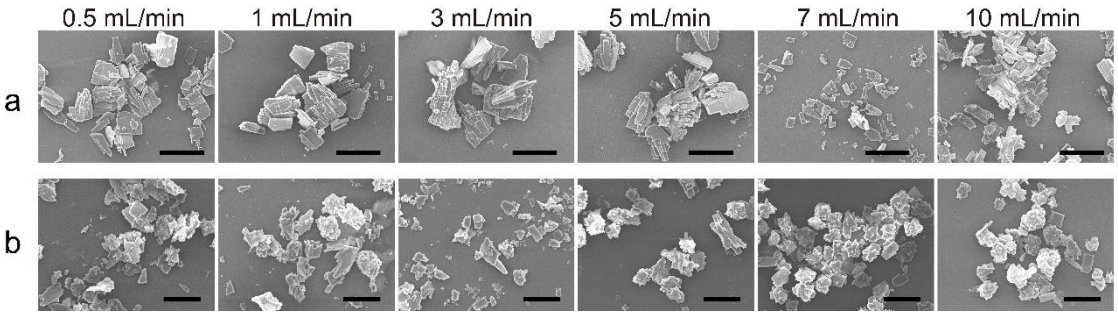

Figure 8. SEM images of CPL-1 crystals synthesized in the Y-shaped reactor with a confluent angle of 40° at various flow rates. The results for $Cu(ClO_4)_2 \cdot 6H_2O$ concentrations of a) 10 mM, and b) 20 mM, which are independent of the flow rate. Scale bars = a) 100 μm, and b) 50 μm.

In contrast, in the case of CPL-2, the crystal size changed with the flow rate and tended to increase as the flow rate increased. The SEM images of CPL-2 shown in Figure 9, reveal that the average size of the crystalline particles synthesized at flow rates of <1 mL/min is ~3 μm, while that of the crystals synthesized at flow rates >5 mL/min are ~10 μm. XRPD results showed that only CPL-2 was obtained by varying the flow rate (Figure 5).

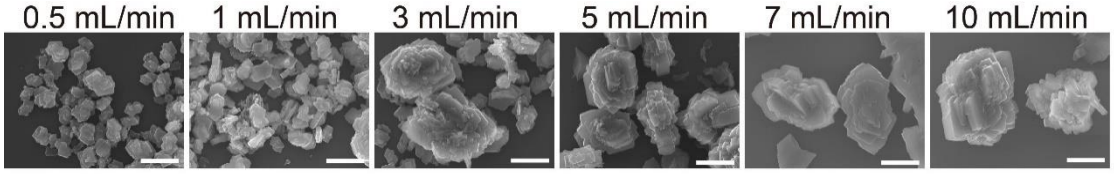

Figure 9. SEM images of CPL-2 crystals synthesized in a Y-shaped reactor with a confluent angle of 40° at various flow rates. Scale bar = 5 μm.

Reasons for the difference of CPL-2 crystal size with flow velocity were discussed. Two possible reasons could be suggested: the difference of the residence time of the solution in the channel or the different solution mixing process at different flow rates.

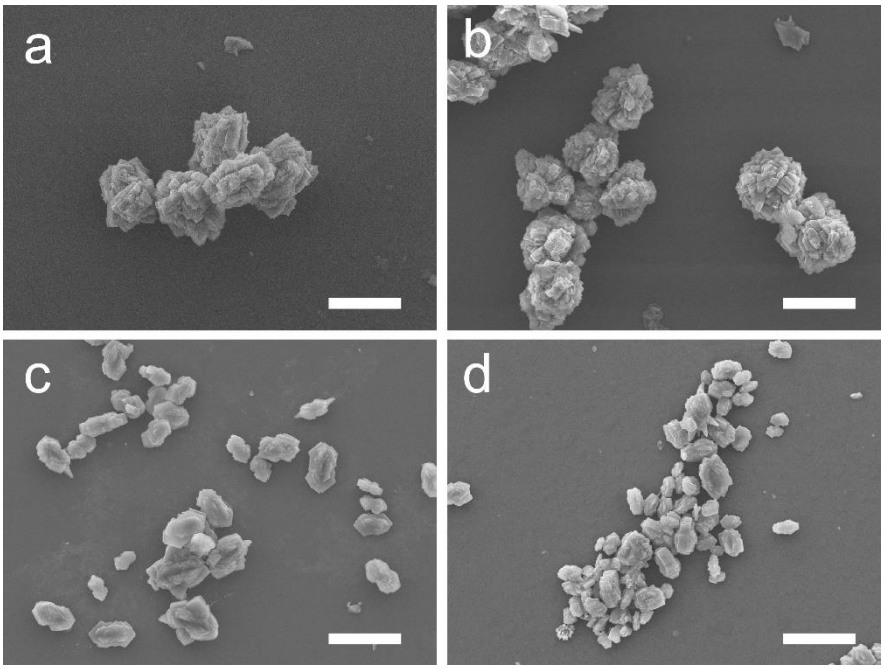

Figure 10. Evaluating the influence of residence time in the microflow reactor. CPL-2 was synthesized with various tube lengths. SEM images of CPL-2 crystals synthesized at a flow rate of 10 mL/min with tube lengths of a) 30 cm, and b) 150 cm, and at a flow rate of 1 mL/min with tube lengths of c) 3 cm, and d) 15 cm. The residence times corresponding to a) and c), and to b) and d) were identical. These results indicate that nucleation is only influenced by mixing efficiency and not residence time. Scale bar = 20 μm.

To evaluate the effect of residence time, the synthesis was performed with different tube lengths. At a flow rate of 10 ml/min, the synthesis was carried out with tube lengths of 30 cm and 150 cm with residence times of 1.4 s and 7.1 s, respectively. In the case of the flow rate of 1 ml/min, the tubes were 3 cm and 15 cm with residence times of 1.4 s and 7.1 s, respectively, to allow comparison for different flow rates at the same residence time. SEM images of the obtained crystals show that the particle sizes are the same at the same flow rate, even if the residence time is different (compare a and b, c and d in Figure 10). It was also found that the flow velocity was different for the same residence time, and crystal size was different (compare a and c, b and d in Figure 10). From these results, it was found that it was not the residence time but the mixing process that affected the particle size.

To investigate how the flow rate and mixing conditions affect the nucleation process, we altered the confluence angle of the microflow reactor. A Y-shaped reactor

(with a 60° confluence angle) and an arrow-shaped reactor (with a 300° confluence angle) were therefore employed for the preparation of CPL-2. The crystallization rate and the CPL-2 crystalline particle size were found to depend on the flow rate, and the flow-rate dependence of the reaction using the arrow-shaped reactor was different to that observed using the Y-shaped reactor (Figure 11a, b). Comparing the crystalline particle sizes at the same flow rate (3 mL/min) revealed that the arrow-shaped reactor produced larger crystalline particles than that produced by Y-shaped reactor.

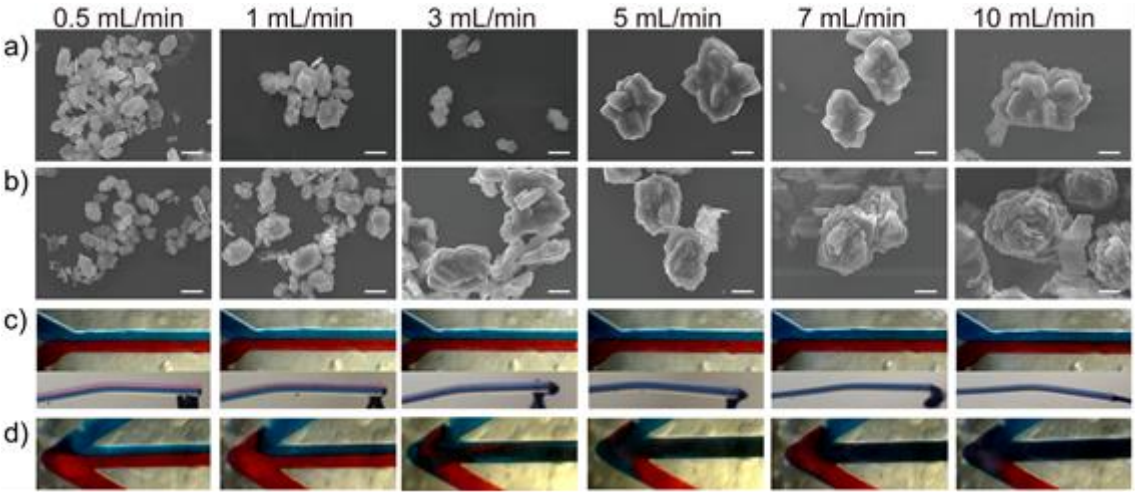

Figure 11. SEM images of the CPL-2 crystals synthesized at various flow rates in: a) a Y-shaped reactor with a confluent angle of 60°, and b) an arrow-shaped reactor with a confluent angle of 300°. Scale bar = 5 μm. The appearance of colored-water mixing in: (c) the Y-shaped reactor (confluent angle of 60°) and the outlet of the tube connected to the microflow reactor 15 cm downstream, and d) the arrow-shaped reactor.

In addition, Aoki et al. reported the relationship between the confluence angle and the mixing conditions, whereby a larger confluence angle increased the mixing efficiency[85]. To evaluate the effect of the reactor shape on the crystallization process, direct observation of the mixing process was performed. Water colored with blue and red dyes was flowed at various rates through each microreactor and observed by optical microscopy (Figure 11c, d). The two solutions were mixed efficiently at a fast flow rate for both shapes of microflow reactor. In contrast, the two solutions flowed separately in a laminar fashion at slow flow rates.

In addition, the difference between the Y-shaped reactor and the arrow-shaped reactor was apparent at an intermediate flow rate. By increasing the concentration of the reaction solution and the rate of crystallization, direct observation of how the solution reacts in the channel was performed.

At 3 mL/min, the solutions in the Y-shaped reactor maintained laminar flow in the flow reactor, while the solution in the arrow-shaped reactor were immediately mixed at the cross point. We also performed a fluid dynamics simulation assuming that mixing is governed only by diffusion (Figure 12). Furthermore, the Reynolds number was <2300 in all cases, which does not correlate with turbulence. However, calculations limited to diffusion processes could not reproduce the results of the colored water experiments, thereby suggesting that the behavior of the liquid at high flow rates cannot be explained in the absence of turbulence.

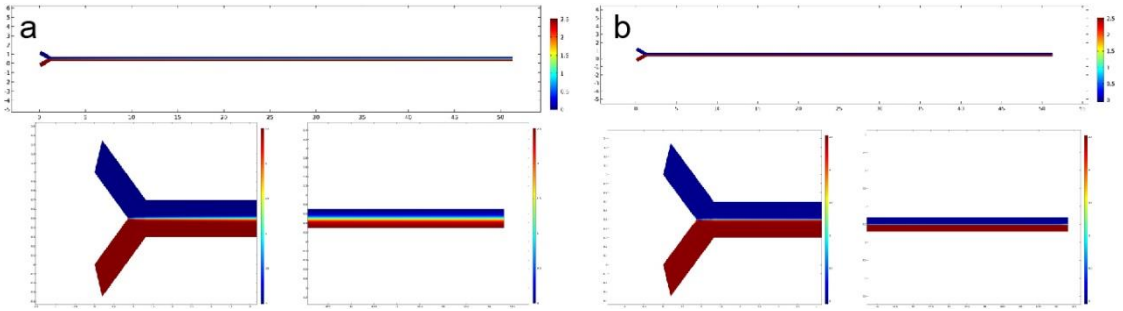

Figure 12. Computational fluidic dynamics (CFD). To calculate the mixing efficiency, CFD was performed at different flow rates for two microflow reactors with different confluence angles. Calculations for the Y-shaped reactor were performed at flow rates of (a) 0.1 mL/min, and (b) 100 mL/min. The results show that the two solutions were mixed at the end of the reactor at the lower flow rate; in contrast, the solutions do not mix at the higher flow rate. However, these calculated data did not match the mixing tendency revealed using colored water. CFD calculations were performed assuming that the solutions mix by diffusion. These calculations reveal that turbulence is more effective than diffusion in a practical setting.

When taken together, the results of these synthesis experiments and the mixing efficiency evaluations indicate that rapid mixing using a stream flow suppresses nucleation and generates larger crystalline particles. Moreover, direct observation of the crystallization process in the flow reactor by optical microscopy revealed that interfacial reactions under laminar flow conditions enhance the nucleation of CPL-2, while rapid mixing under stream flow prevents nucleation (Figure 13). Interestingly, the relationship between the mixing efficiency and the crystalline particle size of CPL-2 observed herein is opposite to that reported by Mae for ZIF-8 in their case, the ZIF-8 crystals became smaller with increasing flow rate[86]. ZIF-8 has been reported to crystallize through a two-step process based on clusters and amorphous nuclei. Our observations are attributed

to the complexity of the CPL-2-crystallization process, which is more complicated than that of ZIF-8 since the latter contains only one type of bridging ligand.

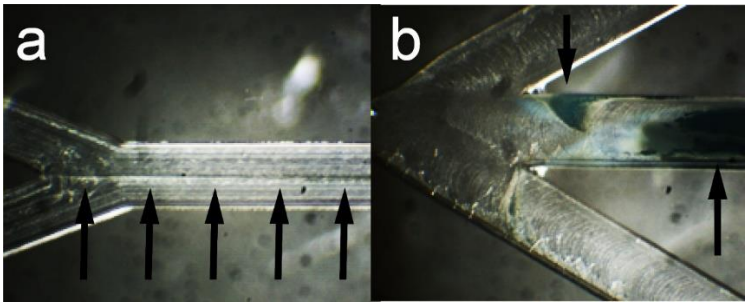

Figure 13. Direct observations of CPL-2 crystallization in a) the Y-shaped, and b) the arrow-shaped microflow reactors at flow rates of 3 mL/min. Inside diameter of both reactors is 400 μm. Precipitated crystals are highlighted by the arrow tips. The fluidic synthesis of CPL-2 at a higher concentration (3.3 mM of $Cu(ClO_4)_2 \cdot 6H_2O$) was performed and the crystallization process in the flow reactor was directly observed by optical microscopy. Under laminar-flow conditions, with a low mixing efficiency, crystals were observed to precipitate at the interface between the two reaction solutions, although under high-mixing-efficiency conditions, such as those in the arrow-shaped reactor at high flow rates, crystals precipitated several micrometers beyond the cross point of the flow reactor, and the distribution of particles in the flow path appeared to be relatively homogeneous. These results suggest that interfacial reactions under laminar-flow conditions enhance CPL-2 nucleation, while rapid mixing under stream flow prevents nucleation.

To investigate the factors that initiate nucleation, we synthesized CPL-1/2 by the stepwise mixing of solutions of Cu ions, pzdc, and the pillar ligand, over two stages (Figure 14). Two arrow-shaped reactors were connected by a 150 mm tube with a 1.0 mm inner diameter, corresponding to a retention time of approximately 0.7 s. Under condition 1, an aqueous solution of $Cu(ClO_4)_2 \cdot 6H_2O$ and an aqueous solution of pzdc were mixed in the first reactor, after which the obtained solution and the solution of pyz/bpy were mixed in the second reactor. The same synthesis, but in reverse order, was carried out under condition 2. Precipitates were obtained by filtration after standing overnight, and these were characterized by XRPD (Figure 15) and SEM (Figure 16).

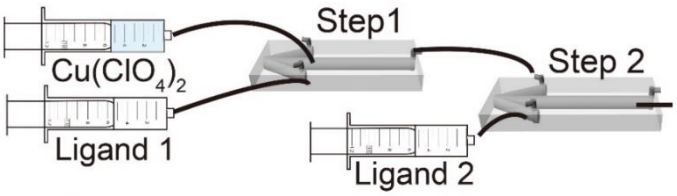

	Step 1	Step 2
Condition 1	$Cu(ClO_4)_2$ + Layer Ligand ($pzdcNa_2$)	+Pillar Ligand (pyz or bpy)
Condition 2	$Cu(ClO_4)_2$ + Pillar Ligand (pyz or bpy)	+Layer Ligand ($pzdcNa_2$)

Figure 14. Schematic representation of the multistep synthesis of CPL-1 and table of mixing condition.

XRPD patterns show that the resulting crystals are all CPL-1/2.

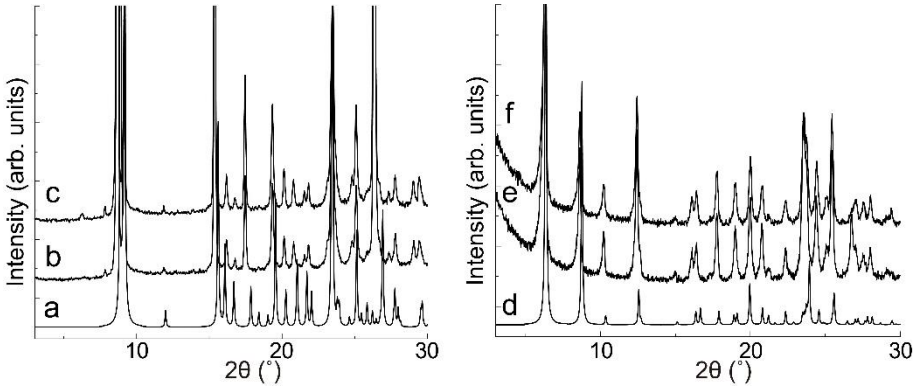

Figure 15. XRPD patterns of CPL-1 and CPL-2 crystals prepared by multistep syntheses. Left: (a) Simulated diffraction pattern of CPL-1 and the XRPD patterns of CPL-1 crystals prepared by multistep syntheses: (b) Condition 1, and (c) Condition 2. Right: (d) Simulated diffraction pattern of CPL-2 and the XRPD patterns of CPL-2 crystals prepared by multistep syntheses: (e) Condition 1, and (f) Condition 2

In the case of CPL-1, under condition 1, the final mixed solution became immediately cloudy, providing small crystalline particles with an average diameter of ~5 μm (Figure 16a). In contrast, crystal precipitation was slower under condition 2, but large crystalline particles with an average diameter of ~20 μm were obtained (Figure 16b).

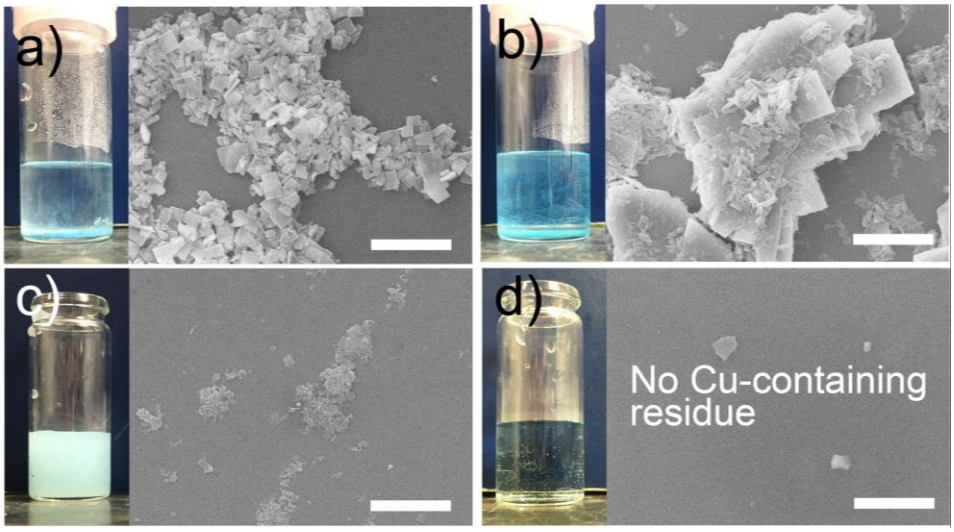

Figure 16. SEM images of the residues when a,c) the $Cu(ClO_4)_2 \cdot 6H_2O$ solution and pzdc solution were mixed first (Condition 1) and b,d) when the $Cu(ClO_4)_2 \cdot 6H_2O$ solution and pyz solution were mixed first (Condition 2) at a,b) at 24 h and c,d) 10 s after the mixing. Scale bar: 20 μm

CPL-2 was then synthesized using the same two procedures, but with bpy instead of pyz, and a similar tendency was observed, i.e., crystals precipitated rapidly when the layer ligand and the copper were mixed first, while crystals precipitated slowly when the pillar ligand and the copper were mixed first (Figure 17). Smaller crystals were obtained in condition 1 and larger ones in condition 2, with the same tendency as in CPL-1.

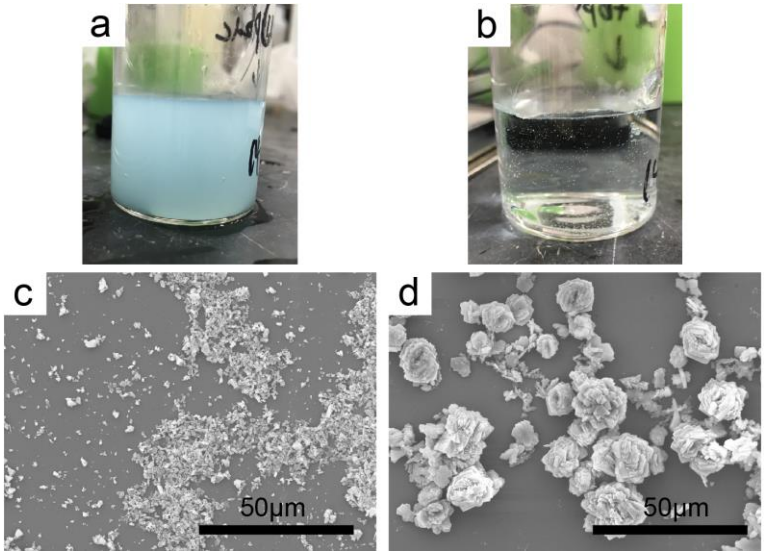

Figure 17. The results from the multistep syntheses of CPL-2. a) The mixed solution obtained when solutions of $Cu(ClO_4)_2 \cdot 6H_2O$ and pzdc were mixed first (Condition 1), and b) the mixed solution obtained when solutions of $Cu(ClO_4)_2$ and 4,4'-bpy were mixed first (Condition 2). The crystals obtained from: c) the solution depicted in a), and d) the solution depicted in b). Similar results were obtained for CPL-1.

The solution after step 1 in Condition 1 was collected to observe whether the reaction mixture becomes cloudy in the first step. The obtained solution was transparent for at least several minutes and no precipitate was obtained by filtration. Multi-step CPL-1 syntheses were also performed in which, the two reactors were connected with 20 mm or 300 mm tubes, corresponding to retention times of approximately 0.1, and 1.3 s, respectively. The particle sizes and morphologies for these two methods were almost identical, indicating that the reaction of Cu^{2+} and pzdc completes immediately upon mixing in the first reactor (Figure 18).

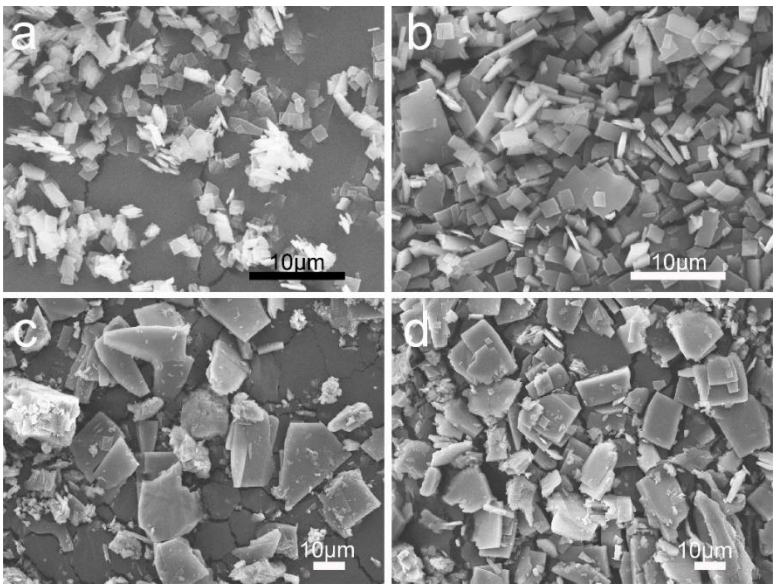

Figure 18. SEM images of the residues obtained by multi step synthesis of CPL-1 in a,b) Condition 1 and c,d) Condition 2 when the tube length between the flow reactors is a,c) 2 cm and b,d) 30cm.

It is suggested that the mixing order affects the nucleation rates of i_{poly}-CPL-1/2, where the nucleation of both species is triggered by the assembly of Cu ions and pzdc. Coordination of the pillar ligand to the Cu ion during the initial mixing prevents the nucleation of i_{poly}-CPL-1/2. These results suggest that pzdc and the pillar ligand play different roles in the crystallization process, whereby pzdc accelerates nucleation and the pillar ligands suppress nucleation. This hypothesis was supported by an experiment employing excess bipyridine and pyridine during the bulk synthesis of CPL-2.

To observe the crystal-precipitation process of CPL-1, the residues filtered at various times (i.e., 10 s, 3 m, 6 h, 9 h, and 24 h) in the multi-step synthesis approach were subjected to SEM (Figure 19) and XRPD (Figure 20). In case of Condition 1, the crystalline particles filtered 10 s after mixing were ~800 nm in size. As the reaction progressed, the residue gradually became larger and eventually grew to ~2 μm. In the case of Condition 2, no Cu-containing residue was observed by energy dispersive X-ray spectroscopy (EDX) for 3 min as the pre-crystal particles were too small to filter or were not generated.

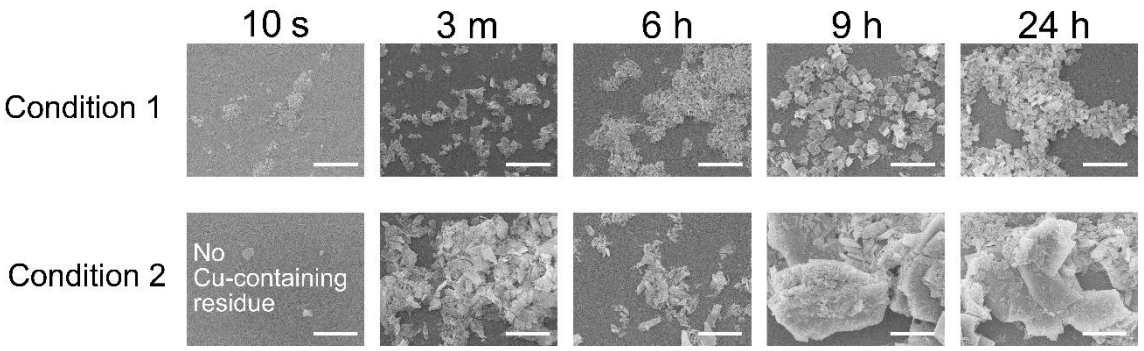

Figure 19. SEM images of the residue filtered at various reaction times during the synthesis of CPL-1 (a) and CPL-2 (b). Scale bar = 10 μm

In addition, the XRPD pattern of the blue residue filtered 10 s after mixing under Condition 1 did not agree with the simulated pattern of CPL-1 (Figure 20a). This result suggests that an intermediate state with a different structure to that of CPL-1 is generated during the crystallization process. Furthermore, when the reaction solution was filtered 10 s after mixing, the polymer intermediate of CPL-1 (hereinafter referred to as "i_{poly}-CPL-1") was isolated. Thereafter, the residue was composed of a mixture of i_{poly}-CPL-1 and CPL-1; the peaks corresponding to i_{poly}-CPL-1 completely disappeared after 24 h and only those of CPL-1 were observed. It was not possible to isolate i_{poly}-CPL-1 under Condition 2, but a similar pattern corresponding to a mixture of CPL-1 and i_{poly}-CPL-1 was observed during the short reaction period. Under these reaction conditions, the diffraction peaks from i_{poly}-CPL-1 remain even after 30 h, suggesting that a longer reaction time is needed to complete CPL-1 formation for Condition 2. These results suggest that both mixing orders produce i_{poly}-CPL-1.

The same procedure was then conducted for CPL-2, which resulted in a different XRPD pattern from the simulated pattern under both mixing conditions, as was observed for CPL-1 (Figures 20c, d). The intermediate of CPL-2 (hereinafter referred to as "i_{poly}-CPL-2") could not be isolated due to the rapid crystallization rate. Although the peaks corresponding to i_{poly}-CPL-2 differed from those of i_{poly}-CPL-1, the apparent correlation between the size of i_{poly}-CPL-1/2 and that of CPL-1/2 allowed us to conclude that CPL-1/2 nucleates at a rate governed by the nucleation of i_{poly}-CPL-1/2. We therefore propose that heterogeneous nucleation (nucleation onto i_{poly}-CPL-1/2 crystals) of CPL-1/2 occurs, and that the formation of i_{poly}-CPL-1/2 microcrystal is required for the formation of CPL-1/2. It is most likely that i_{poly}-CPL-1/2 is converted into CPL-1/2 directly or through dissolution-recrystallization processes. The faster i_{poly}-CPL-1/2 formation results in a higher nucleus concentration, leading to smaller crystalline particles of CPL-1/2.

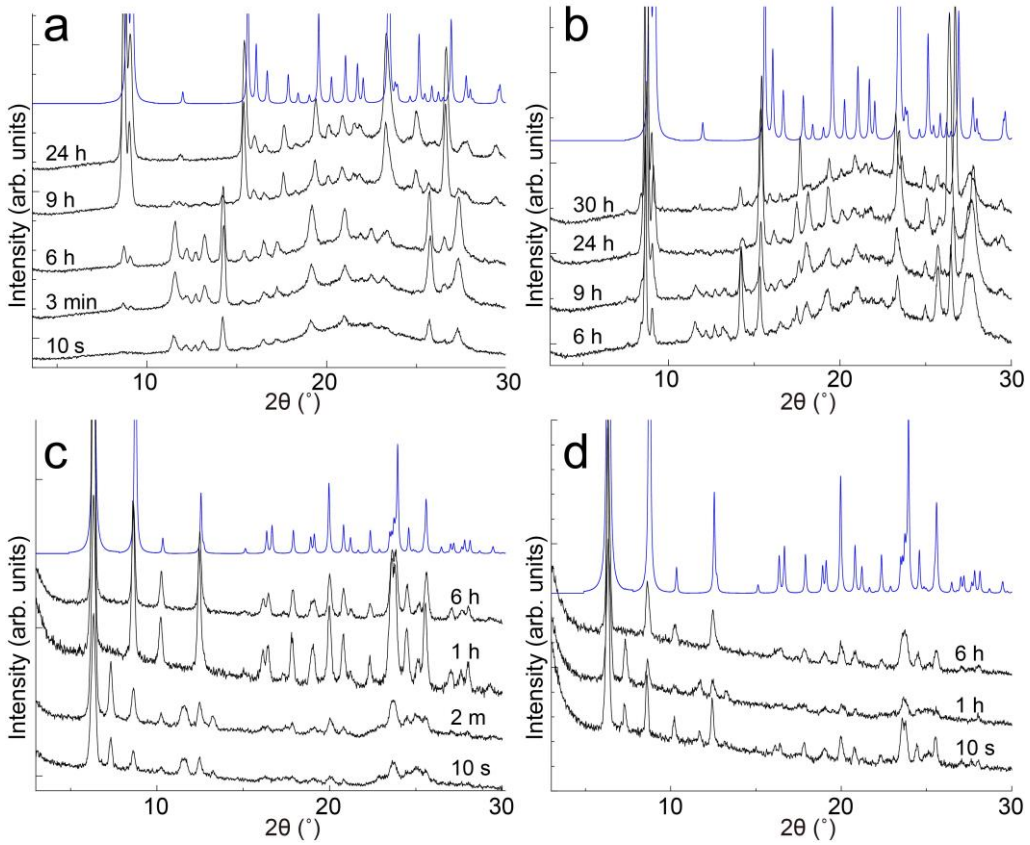

Figure 20. XRPD patterns of the residues filtered at different reaction times. a), b) CPL-1, and c), d) CPL-2. a), c) Condition 1, and b), d) Condition 2. The simulated patterns are shown in blue.

Next, the characterization of the structure of i_{poly}-CPL-1 by elemental analysis, infrared (IR) spectroscopy, and thermogravimetric (TG) analysis, was performed. The carbon/nitrogen ratio evaluated from the elemental analysis suggests that the pzdc/pyz ratio in i_{poly}-CPL-1 is 1.8, which is close to that in CPL-1 ($Cu_2(pzdc)_2(pyz)\cdot 2H_2O$) (Table 1).

Table. Comparison of elemental analysis results for i_{poly}-CPL-1 with the theoretical values of CPL-1. C/N calcd for [(pzdc)1.8pyz] is 2.27.

	C %	H %	N %	C/N
Experimental interemeditate	31.94	1.81	14.09	2.27
Theoretical $Cu_{2.4(}pzdc)_{1.8}pyz\cdot H_2O_{1.5}$	31.81	1.90	14.04	2.27

IR spectroscopy also confirmed the inclusion of both ligands in i_{poly}-CPL-1 (Figure 21).

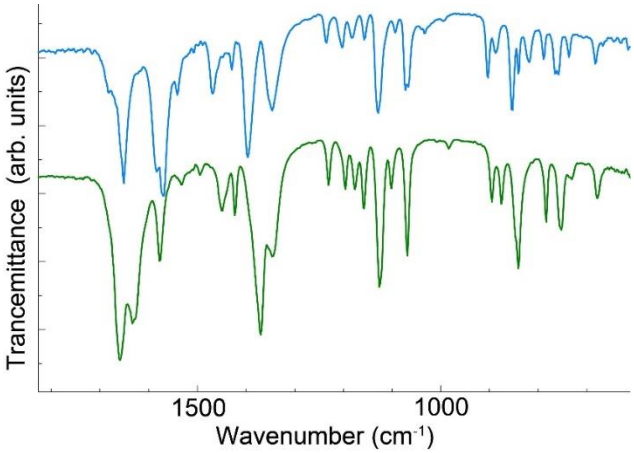

Figure 21. IR spectra of i_{poly}-CPL-1 (green) and CPL-1 (blue).

In addition, a blue-to-green color change was observed when i_{poly}-CPL-1 was dried under vacuum at 100 °C. Upon exposure to water vapor, the dehydrated green i_{poly}-CPL-1 regained its blue color. The XRD pattern of i_{poly}-CPL-1 is changed after drying, as shown in Figure 22, which suggests that crystal structure transformation occurs upon water removal at high temperature.

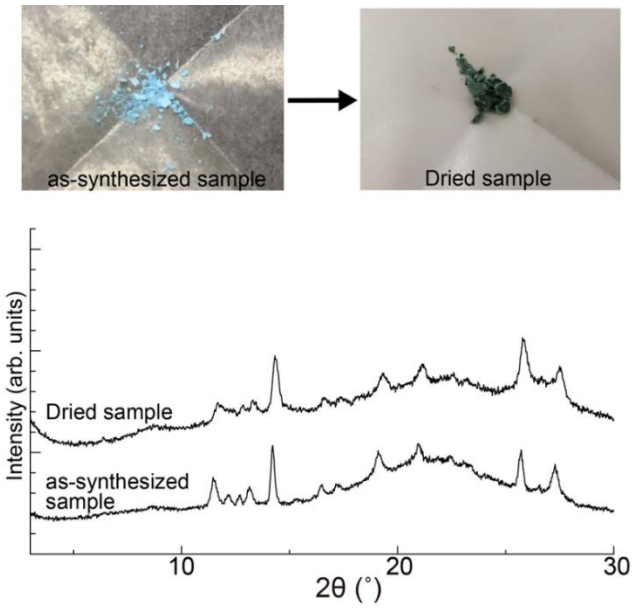

Figure 22. Optical images and XRPD patterns of the dried and as-synthesized i_{poly}-CPL-1.

We therefore conclude that water molecules are present in the structure of i_{poly}-CPL-1. This was also confirmed by TG analysis (Figure 23).

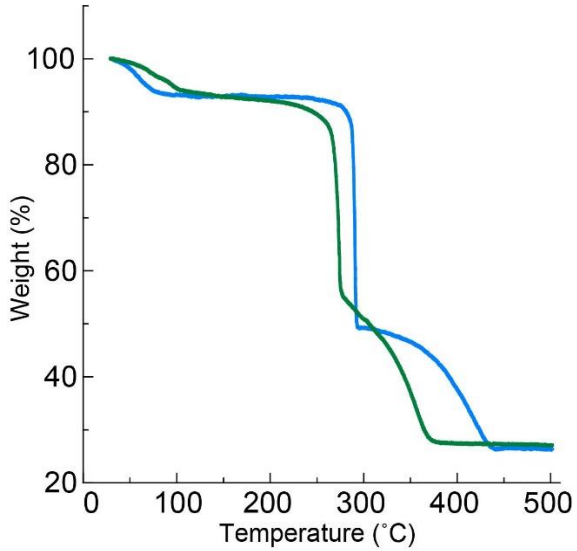

Figure 23. TG analysis of i_{poly}-CPL-1 (green) and CPL-1 (blue).

These results suggest that the coordination structure of i_{poly}-CPL-1 differs from that of CPL-1, but that they have similar compositions.

2-2-3. In-situ flow spectroscopic measurements

Next, we focused on the changes in the local structure during the reaction. To characterize the changes in the local coordination structure of Cu ions during crystallization, samples in four states were subjected to UV-vis and X-ray absorption spectroscopy. These states included an aqueous $Cu(ClO_4)_2 \cdot 6H_2O$ solution as the initial reaction state, CPL-1/2 crystals as the final state, and the supersaturated solution containing a mixture of the reactant solution and the i_{poly}-CPL-1 pellet as the intermediate (Figure 24). The mechanism is discussed in terms of the CPL-1 spectra since a smooth spectrum could not be obtained for the supersaturated solution of CPL-2, and i_{poly}-CPL-2 could not be isolated.

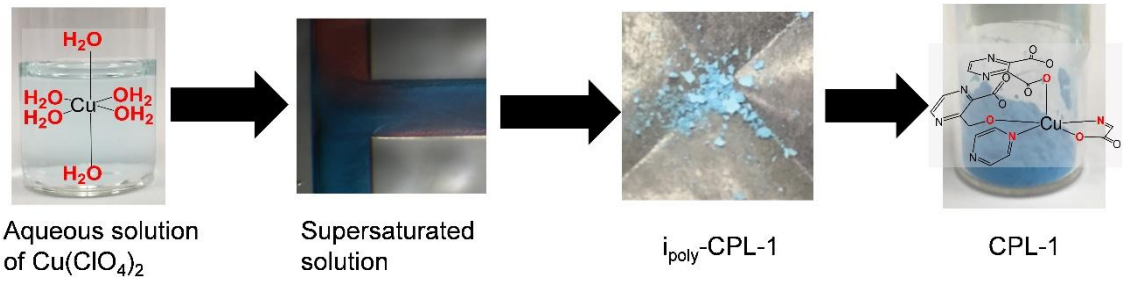

Figure 24. Four samples for the spectroscopic measurements

To evaluate the state of the supersaturated solution, we prepared an in-situ flow measurement cell. Because the supersaturated state changes towards the equilibrium state over time and crystals quickly precipitate, a setup for regularly observing the state immediately after the start of the reaction is necessary. We developed an in-situ flow measurement method that combines microfluidics and spectroscopy. In this system there is a correlation between the reaction time and the distance from the microchannel to the flow cell, so that a constant reaction state can be continuously evaluated by observing the solution flowing at a certain position in the flow cell. This method was adopted to UV-vis and X-ray absorption spectroscopy.

The setup for UV-vis spectroscopy is shown in Figure 25. A commercial flow cell was used for this measurement.

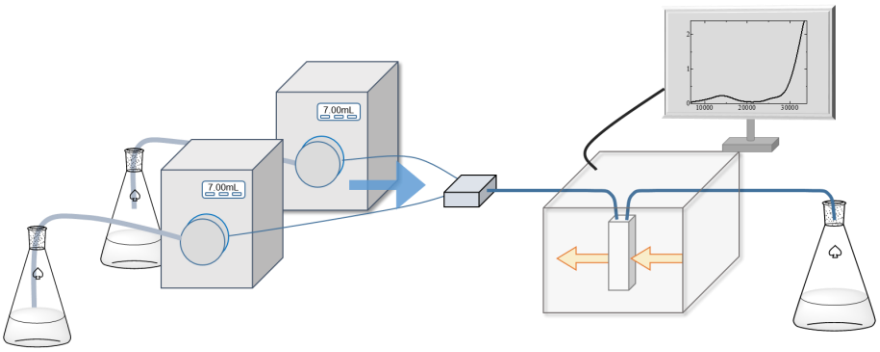

Figure 25. The set-up employed for in-situ UV-Vis absorption measurements. A fluidic-synthesis system equipped with dual-head pumps (YMCK-24-13, YMC) for in-situ flow experiments was used. The exit of the T-shaped microreactor, with a 500 μm inner diameter (YMC-P-0058, YMC), was connected to a flow cell (Hellma Analysis, Precision cells) with a thermoelectric single cell holder (SHIMADZU S-1700) to control the temperature at 25 °C and facilitate the direct observation of the flowing mixture.

For XAFS measurements, a flow cell was prepared and the measurements were performed at BL14B2 at SPring-8 (Figure 26). The solutions were mixed using the T-shaped reactor (silver-colored box on the left side), and flowed through the PEEK tube. A transparent acrylic cell holder (in the center) was used to settle the tube by binding with a clamp.

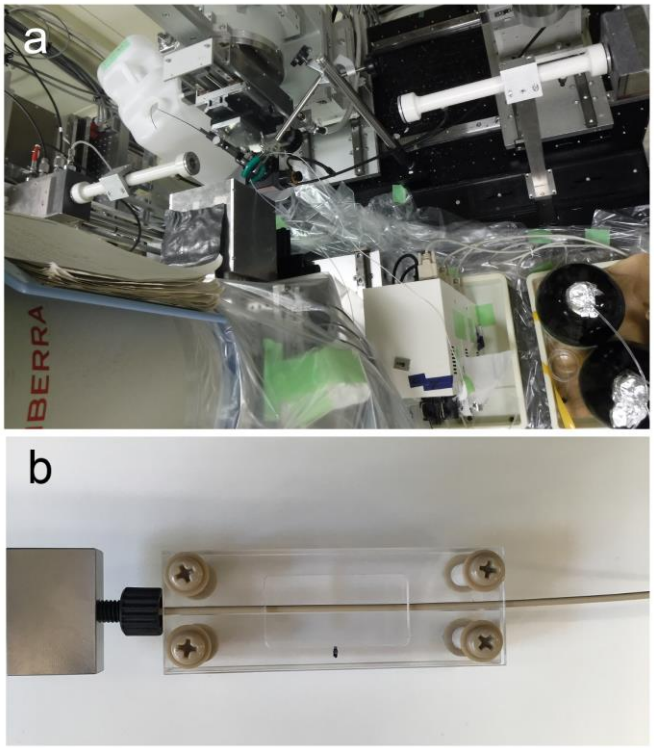

Figure 26. The set-up employed for in-situ XAFS experiments performed on the BL14B2 beamline at SPring-8. (a) The microfluidic system for in-situ XAFS experiments. The syringe pumps or dual-head plunger pumps and the glass bottles that contain the solutions are held on the right side (the plunger pumps are shown in the image. The plunger and syringe pumps are used for the syntheses of CPL-1 and 2, respectively). The microflow reactor and the flow cell are connected to the pumps. The X-ray beam enters from the cylinder on the left and fluorescence is detected by the detector at the front. (b) Depiction of the flow cell.

UV-vis absorption spectra of four measured samples are shown in Figure 27a. Gaussian fitting of the UV-Vis absorption spectra showed that the peak position and the relative intensity relationships for the supersaturated solution (i.e., 6262 and 14002 cm^{-1}, corresponding to 1597 and 714 nm, respectively) and i_{poly}-CPL-1 (8609 and 13878 cm^{-1}, corresponding to 1162 and 721 nm, respectively) are similar (Figures 27c and 27d). These peaks do not correspond to the Gaussian peaks of the aqueous solution of $Cu(ClO_4)_2$(i.e., 11633 and 12846 cm^{-1}, corresponding to 860 and 778 nm, respectively) or CPL-1 (13846 and 15466 cm^{-1}, corresponding to 772 and 647 nm, respectively), indicating that the coordination structures of the coordination compound in the supersaturated solution and i_{poly}-CPL-1 are similar but differ from those of the initial and

final states (Figures 27b and 27e). Hereafter, we refer to the copper ion in the supersaturated solution as "i_{sol}-CPL-1" (i.e., the CPL-1 intermediate in solution).

In order to determine the local coordination structures, XAFS experiments were then performed on the same samples employed in the UV-Vis absorption study (Figure 27f). However, the CPL-1 spectra of i_{sol}-CPL-1 acquired using the in situ fluidic system were not sufficiently smooth in the EXAFS region for quantitative analysis. We therefore focused on the spectrum of CPL-1 in the X-ray-absorption near-edge structure (XANES) region. The noisy CPL-2 spectra exhibited similar tendencies (Figure 28a).

The XAFS spectra and their Fourier transforms were found to display small differences between the four samples, although all spectra were characteristic of Cu(II). In situ spectra of i_{sol}-CPL-1 were acquired 35, 150, and 300 mm beyond the exit of the flow reactor, which correspond to reaction times of approximately 0.2, 1.0, and 2.0 s, respectively. These three spectra matched completely, indicating that i_{sol}-CPL-1 in the non-equilibrium state is sufficiently stable under our measurement conditions (Figure 28b). Furthermore, the XANES spectra of two model complexes, i.e., a pellet of Cu(II) and a pzdc coordination polymer, $[Cu(pzdc)_2(H_2O)]$, and an aqueous solution of $Cu(ClO_4)_2 \cdot 6H_2O$ with pyz, were also acquired. The spectra of the model compounds do not correspond well with that of i_{sol}-CPL-1, thereby suggesting that the i_{sol}-CPL-1 present in the supersaturated solution is composed of both pzdc and pyz, as well as water molecules, as was observed for i_{poly}-CPL-1 (Figures 28c and 28d). In contrast, the pre-edge peak positions (8978 eV) in the spectra of i_{sol}-CPL-1, i_{poly}-CPL-1, and CPL-1 are similar and slightly shifted from that of aqueous $Cu(ClO_4)_2 \cdot 6H_2O$ (Figure 27f). Pre-edge peaks are known to depend on the symmetry of the metal-ion coordination structure[87-90]; hence, these results suggest that the Cu ions in i_{sol}-CPL-1 and i_{poly}-CPL-1 give analogous coordination compounds whose symmetries are similar to that of CPL-1, but whose structures differ from that of CPL-1, as shown by UV-Vis absorption spectroscopy.

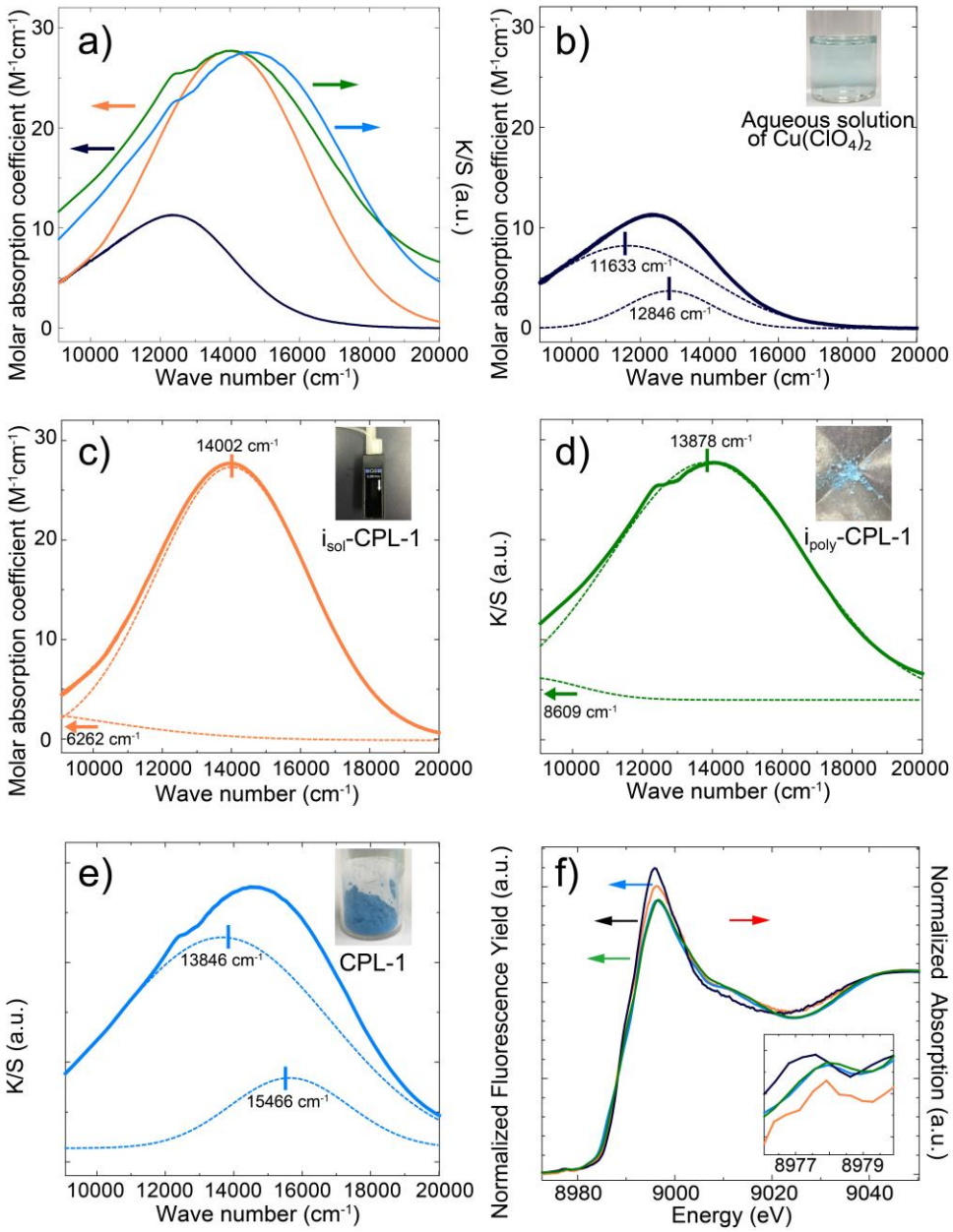

Figure 27. UV-vis absorption and XAFS spectra. a) UV-vis absorption spectra of an aqueous solutions of $Cu(ClO_4)_2 \cdot 6H_2O$ (black), the CPL-1 pellet (blue), the supersaturated solution (i_{sol}-CPL-1) (orange), and the isolated i_{poly}-CPL-1 (green). Fitting peaks of b) an aqueous solution of $Cu(ClO_4)_2 \cdot 6H_2O$, c) i_{sol}-CPL-1, d) the pellet of i_{poly}-CPL-1 and e) the pellet of CPL-1. f) The XANES regions of the normalized Cu-K edge XAFS spectra. Samples corresponding to the color of the UV-vis absorption spectra are shown. The inset displays expanded views of the pre-edge regions. Fourier transformed spectra are shown in Figure. 29

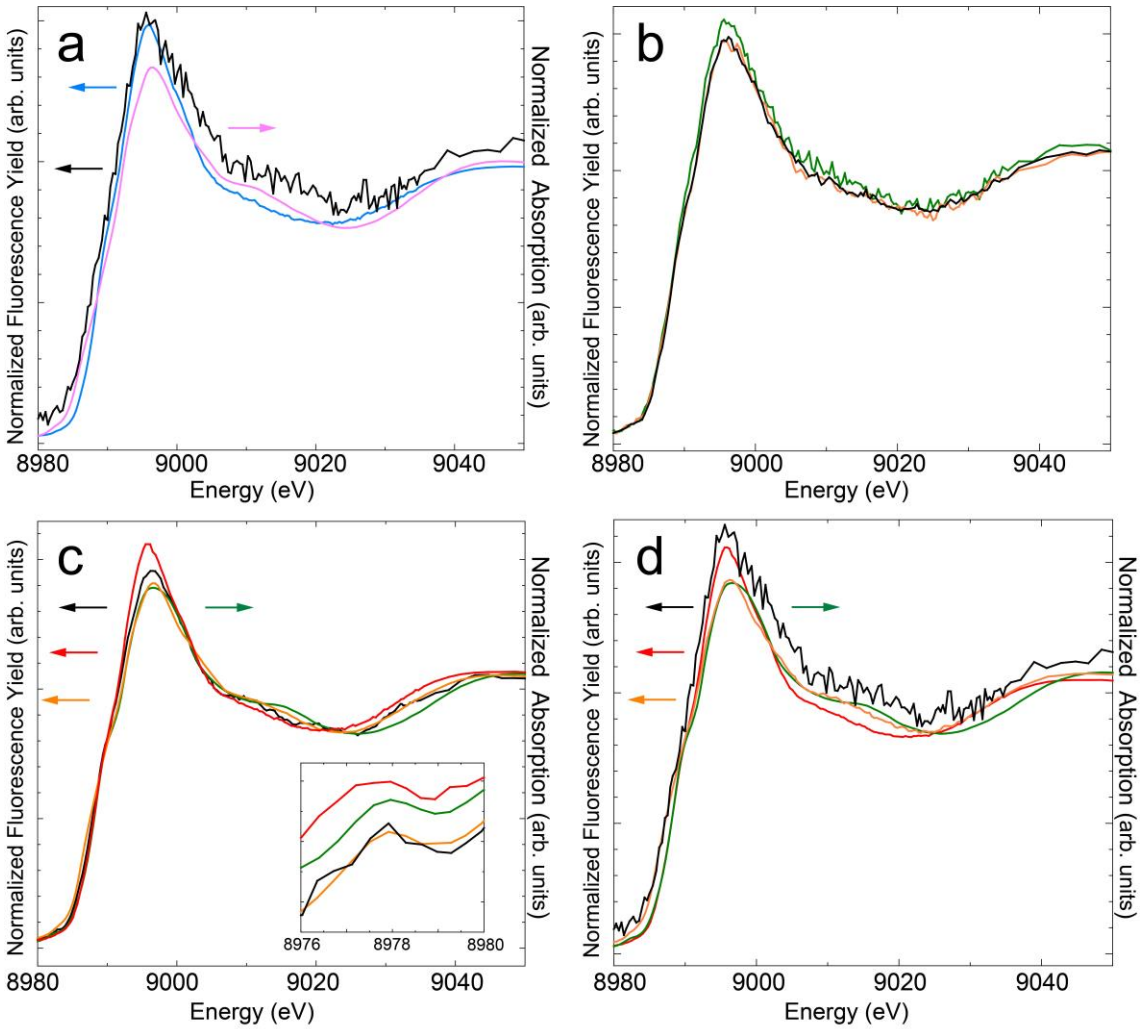

Figure 28. XAFS spectra. (a) XANES region of the XAFS spectra for an aqueous solution of $Cu(ClO_4)_2 \cdot 6H_2O$ (blue), a CPL-2 pellet (pink), and the mixed CPL-2 solution (black). (b) The spectra of the mixed CPL-1 solution acquired at the three different positions were identical (the distances between the microflow reactor and the acquisition position were 3.5 (black), 15 (orange), and 30 cm (green), corresponding to reaction times of approximately 0.2, 1.0, and 2.0 s, respectively). The in-situ spectra of supersaturated solutions of (c) CPL-1, and (d) CPL-2 (black) and the model samples: a pellet of the Cu2+ and pzdc crystals (green, see Figure 30), a mixed solution of $Cu(ClO_4)_2 \cdot 6H_2O$ and pyz (red), and a mixed solution of $Cu(ClO_4)_2 \cdot 6H_2O$, pzdc, and pyridine (orange)

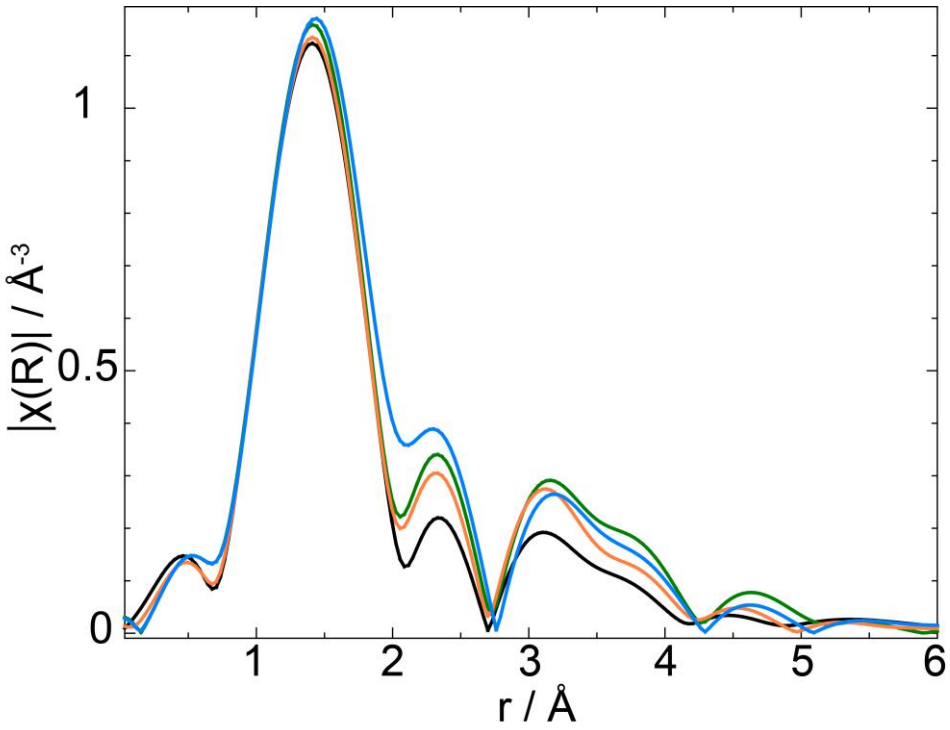

Figure 29. Fourier-transformed XAFS spectra of an aqueous solution of $Cu(ClO_4)_2 \cdot 6H_2O$ (black), the CPL-1 pellet (blue), the supersaturated solution (i_{sol}-CPL-1) (orange), and the isolated i_{poly}-CPL-1 (green).

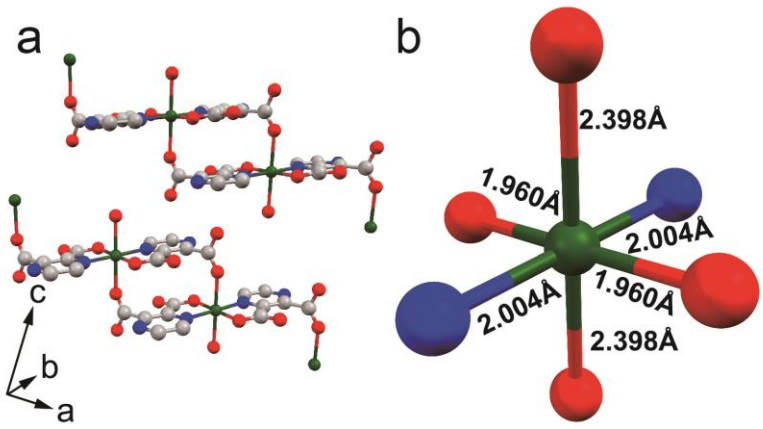

Figure 30. The reported crystal structure of the model sample, $[Cu(pzdc)_2(H_2O)]$. (a) Crystal structure of the network, and (b) the local coordination structure[91]. O red, N blue, and Cu green.

2-2-4. Proposed crystallization mechanism

Based on the previous fluidic experiments, we propose a crystallization process for CPL-1/2 that takes place over three steps and can be considered to be a typical secondary nucleation process (Figure 30a). It is known that many MOFs crystallize via sequential rather than one-step-nucleation crystal-growth processes, which are generally known as Ostwald's Rule of Stages. In step 1, i_{sol}-CPL-1/2 is generated rapidly (within 0.05 s). Although both pzdc and the pillar ligand coordinate to the copper ion in i_{sol}-CPL-1/2, the coordination structure of i_{sol}-CPL-1/2 differs from that of the aqueous solution of $Cu(ClO_4)_2$ and CPL-1/2. At this point, the coordination symmetry becomes penta-coordinated square pyramidal, similar to that of CPL-1/2. In step 2, i_{sol}-CPL-1/2 crystalizes while maintaining the coordination environment, resulting in the precipitation of i_{sol}-CPL-1/2. The multi-step synthesis process revealed that the activation energy in this process depends on the ease of formation of the Cu-pzdc assembly during the initial reaction period (Figure 30b). When the pillar ligands are initially present in the reaction solution, heteroaromatic amine pillars stabilize the metastable intermediate structure in solution (i_{sol}-CPL-1/2), suppressing step 2 and resulting in the slow nucleation of i_{poly}-CPL-1/2 or a relatively stable supersaturated solution. It therefore appears that the two kinds of ligand play different roles in the crystallization process, thereby rendering the mechanism of pillared-layer MOF formation rather complicated. Finally, in step 3, i_{poly}-CPL-1/2 is converted into CPL-1/2 while maintaining the coordination symmetry through solid-phase rearrangement or dissolution-recrystallization processes. i_{sol}-CPL-1/2 in the solution is also consumed for the crystal growth of CPL-1/2. In the proposed crystallization mechanism, heterogeneous nucleation (nucleation onto i_{poly}-CPL-1/2 crystals) occurs, and the formation of i_{poly}-CPL-1/2 microcrystal is required for the formation of CPL-1/2. In this crystallization model, i_{poly}-CPL-1/2 is converted into CPL-1/2 directly or through dissolution-recrystallization processes on the i_{poly}-CPL-1/2 crystals. When CPL-1/2 formation does not proceed by anisotropic crystallization, such as single-crystal to single-crystal transformation and epitaxial growth, CPL-1/2 grows isotropically from a seed center of i_{poly}-CPL-1/2 in various directions, resulting in particles with morphologies that resemble single-crystal aggregation.

This hypothetical nucleation mechanism is consistent with the bulk synthesis results, in which CPL-2 crystals synthesized using excess amounts of bpy and pyridine were observed to be larger than CPL-2 crystals synthesized using an equivalent amount of bpy, as described above. This result can be accounted for by considering the excess bpy

and pyridine present in the CPL-2 synthesis process, which stabilizes i_{sol}-CPL-2 and suppresses the nucleation of i_{poly}-CPL-2.

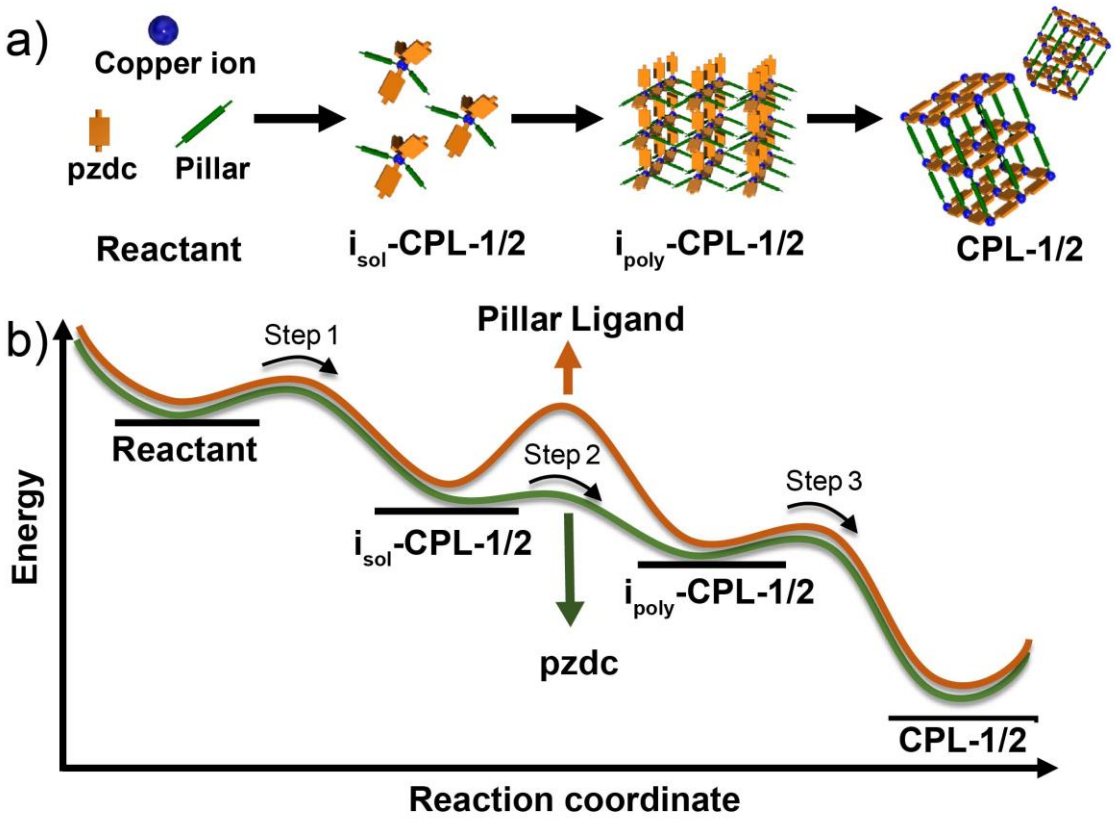

Figure 31. Proposed three step crystallization process and b) the corresponding energy diagram.

2-3. Conclusion

Herein, we proposed a crystallization mechanism for CPL-1/2, which are pillared-layer MOFs, based on non-classical crystallization processes involving two kinds of intermediate state. To the best of our knowledge, this is the first report that details the roles of these two kinds of ligand in the nucleation processes of pillared-layer MOFs, which we believe will open up further mechanistic studies into the crystallization behavior of multi-component MOFs. We also confirmed that the microflow reactor is a valuable tool for evaluating non-equilibrium states, enabling the reaction solution to be observed directly and the intermediate to be isolated in the initial period, ultimately resulting in the elucidation of the complex mechanism.

2-4. Experimental section

General

All reagents were obtained from commercial suppliers and were used without further purification. Pyrazine and pyridine were obtained from WAKO Pure Chemical Industries, Ltd., $Cu(ClO_4)_2 \cdot 6H_2O$ was obtained from the Kanto Chemical Co., Inc., while bipyridine, 2,3-pyridinedicarboxylic acid, and NaOH were obtained from Tokyo Chemical Industry Co., Ltd. Sodium 2,3-pyrazinedicarboxylate was prepared by dissolving 2,3-pyrazinedicarboxylic acid (5.0 g) in an aqueous solution of NaOH (2.5 M, 25 mL). After stirring for 2 h, the solution was poured into methanol (25 mL) and the precipitate was collected by filtration and dried under vacuum. XRPD patterns were collected on a Rigaku RINT-2000 or Rigaku Mini Flex 600 diffractometer with CuKα radiation. It is known that the XRD patterns of CPL-1/2 change by the adsorption or removal of water in the pores. Although we measured the XRD patterns after vacuum drying, the amount of water in the pores depends on the ambient moisture and experimental conditions, resulting in slight shifts in the XRD signals.[1] SEM and EDX were performed using a JEOL JSM-7001FA or JCM-6000 microscope. Crystals were coated with osmium or gold for the purpose of SEM observations.

Bulk syntheses of CPL-1 and CPL-2

The bulk syntheses of CPL-1/2 were performed according to reported procedures.

Synthesis of CPL-1: Na_2pzdc (0.03 g, 10 mM) in H_2O (15 mL) was slowly added to a solution of $Cu(ClO_4)_2 \cdot 6H_2O$ (0.06 g, 10 mM) and pyz (0.15 g, 124 mM) in water (15 mL) using a dropping funnel and a staller. After stirring for 3 h, the mixture was subjected to centrifugation, and the blue crystals were collected and washed twice with methanol. The crystals were then subjected to XRPD and SEM after drying under vacuum.

Synthesis of CPL-2*:* $Cu(ClO_4)_2 \cdot 6H_2O$ (0.19 g, 10 mM) in H_2O (50 mL) was slowly added to a solution of Na_2pzdc (0.11 g, 10 mM) and bpy (0.05 g, 6.0 mM) in 1:1 methanol:water (50 mL). After stirring for 3 h, the mixture was subjected to centrifugation, and the blue crystals were collected and washed twice with methanol. The crystals were then analyzed after drying under vacuum.

Fabricating microflow reactors for fluidic synthesis

Microfluidic patterns were fabricated on poly(methyl methacrylate) (PMMA) using a computer numerically controlled (CNC) micro-milling system (MM-100, Modia Systems) with a rigid drill bit with a tip diameter of 0.2 mm (NS tool). Subsequently, microchannels

were assembled by bonding the PMMA sheet milled with the microchannel pattern and the PMMA substrate by thermal compression. All microchannels channel were 400 μm wide and deep.

One-step microfluidic syntheses of CPL-1 and CPL-2

Microfluidic syntheses were carried out using a microflow reactor with confluent angles of 40, 60, and 300°. Two 10 mL HSW Norm-Ject® all-plastic disposable syringes (Luer-lock version) were filled with a mixed solution (10 mL) of $Cu(ClO_4)_2 \cdot 6H_2O$ (1.3–20 mM) and pyz (16.1–248 mM), and sodium 2,3-pyrazinedicarboxylic acid (1.3–20 mM) for CPL-1, and an aqueous solution of $Cu(ClO_4)_2 \cdot 6H_2O$ (1.3–20 mM, 10 mL) and a mixed solution (10 mL) of sodium 2,3-pyrazinedicarboxylic acid (1.3–20 mM) and 4,4'-bipyridine in methanol (0.8–12 mM) for CPL-2, after which they were pumped into the reactor through 1-mm diameter tubes by two syringe pumps (YMC YSP-201). The mixed solution was allowed to stand for ~12 h, after which time the precipitate was separated by centrifugation or filtration (depending on the crystal size) and washed twice with methanol, as described in the bulk synthesis procedure. Each series of experiments was performed using the same mother solutions to evaluate the effect of the experimental parameters, such as flow rate.

Qualitatively evaluating mixing efficiency using colored water

The effect of the confluence angle on the mixing efficiency at various flow rates was evaluated according to the following procedure. Blue and red dyes (the pigments were supplied by Kyoritsu foods) were dissolved in water and a mixed water/methanol solution, respectively. Optical images were acquired during flow.

Multistep fluidic syntheses of CPL-1 and CPL-2

Multistep fluidic syntheses were carried out using two arrow-shaped microflow reactors connected by a 15 cm tube with a 1.0 mm inner diameter. An aqueous solution of $Cu(ClO_4)_2 \cdot 6H_2O$ (10 mM, 10 mL), an aqueous solution of Na_2pzdc (20 mM, 5 mL), and pyz in methanol (250 mM, 10 mL) were prepared for the synthesis of CPL-1. An aqueous solution of $Cu(ClO_4)_2 \cdot 6H_2O$ (2.5 mM, 5 mL), an aqueous solution of Na_2pzdc (5.0 mM, 5 mL), and bpy in methanol (3.1 mM, 5 mL) were prepared for the synthesis of CPL-2. An aqueous solution of $Cu(ClO_4)_2 \cdot 6H_2O$ and pyz, and a separate aqueous solution of pzdc were used for CPL-1, while a water/methanol solution of pzdc and bpy, and a separate aqueous solution of $Cu(ClO_4)_2 \cdot 6H_2O$ were used for CPL-2. The flow rates of the two solutions were identical in each case, and were adjusted using syringe pumps to be in

the 0.5–10 mL/min range. Although the concentration of the $Cu(ClO_4)_2 \cdot 6H_2O$ solution varied from 1.3 to 20 mM, the metal/ligand molar ratio was identical to that used in the reported bulk syntheses. Three syringes, each filled with the corresponding solution, were prepared. The mixed solutions were left to stand overnight to complete the crystallization process. Each series of experiments was performed using the same mother solutions to evaluate the effect of the experimental parameters, such as flow rate, order of mixing, and retention time.

Isolation of i_{poly}-CPL-1

i_{poly}-CPL-1 was isolated using the same setup as that employed for the multi-step synthesis. All pumps were started after the tubes containing the three solutions were emptied, and solution collection was begun. The collection start time was set to 0 s, and the mixed solution was collected for 3 s. Filtration was performed at an arbitrary time from the start of fractionation using a membrane filter (Omnipore PTFE 0.25 μm). The residue was then washed with ~15 mL of methanol. To remove the residue from the membrane filter, the residue was immersed in methanol and ultrasonicated for ~5 min. The solvent of the supernatant solution was removed by centrifugation and the residue was dried overnight at room temperature.

UV-vis absorption spectroscopy

· **Solid state:** A solid sample pellet was prepared by mixing barium sulfate and the solid sample in a mass ratio of approximately 10:1. During examination with a UV-3600 Plus instrument, switching of the detector wavelength was adjusted to 720 and 1650 nm, and that of the grating was adjusted to 700 nm. A slit width of 20 mm was also employed.

· **Liquid sample:** All liquid samples were prepared using volumetric flasks. The liquid samples (with the exception of the fluidic experiments) were examined using a UV-3600 plus instrument (0.2 mm slit width), while the fluidic experiments were carried out using a UV-1800 instrument (1.0 nm slit width). The in-situ experimental set-up is shown in Figure 25.

All Gaussian fitting procedures were carried out using Origin by the LightStone Corp.

X-ray absorption spectroscopy (XAS)

XAS was performed at the BL14B2 beamline of the SPring-8 facility (Hyogo, Japan). Si (311) monochromator crystals were used to scan energies above the Cu K-edge. Crystal pellets of CPL-1 and CPL-2 were examined in transmission mode using ionization

chambers. Fluorescence spectra were recorded using a 19-element solid-state Ge detector to characterize dilute solution samples. A fluidic-synthesis system equipped with dual-head pumps (YMCK-24-13, YMC) for in-situ CPL-1 experiments, or syringe pumps (YSP-201, YMC) for other experiments, was used. The exit of the T-shaped microreactor, with a 500 μm inner diameter (YMC-P-0058, YMC), was connected to a PEEK tube with a 1.4 mm inner diameter (VICI Jour) to facilitate the direct observation of the flowing mixture. The PEEK tube was settled with an acrylic cell holder. The beam-spot size was 1.5 mm, and its center was positioned at the center of the PEEK tube. The detailed setup is shown in Figure 26. The obtained XAFS spectra were normalized and background scattering was subtracted by data processing using Athena 0.9.25 software[92].

Bulk synthesis of CPL-2 with excess pyridine

A solution of bpy (0.05 g, 6.0 mM) in 1:1 methanol:water (50 mL) was slowly added to an aqueous solution (50 mL) of $Cu(ClO_4)_2 \cdot 6H_2O$ (0.19 g, 10 mM), Na_2pzdc (0.11 g, 10 mM), and pyridine (80 mM). After stirring for 3 h, the mixture was subjected to centrifugation, and the blue crystals were collected and washed twice with methanol. The crystals were analyzed after drying under vacuum.

Preparing the XAFS solutions used in Figure 30

Mixed solution of $Cu(ClO_4)_2 \cdot 6H_2O$ and pyz

$Cu(ClO_4)_2 \cdot 6H_2O$ (12.5 mM) and pyz (156 mM) were dissolved in water (10 mL). The flow-measurement system was filled using a syringe pump, and the flow was stopped during the acquisition of data.

Mixed solution of $Cu(ClO_4)_2 \cdot 6H_2O$, pzdc, and pyridine

An aqueous solution of $Cu(ClO_4)_2 \cdot 6H_2O$ (10 mM, 10 mL) and pyz (80 mM), and an aqueous solution of pzdcNa2 (10 mM, 10 mL) were prepared. The two solutions were mixed as described for the CPL-1 in-situ flow experiments, and the flow was stopped during data acquisition.

2-5. Reference

74. Dybtsev, D. N.; Chun, H.; Kim, K., Rigid and flexible: a highly porous metal-organic framework with unusual guest-dependent dynamic behavior. *Angew. Chem. Int. Ed.* **2004,** *43* (38), 5033-6.

75. Cho, S. H.; Ma, B. Q.; Nguyen, S. T.; Hupp, J. T.; Albrecht-Schmitt, T. E., A metal-organic framework material that functions as an enantioselective catalyst for olefin epoxidation. *Chem. Commun.* **2006,** (24), 2563-2565.

76. Henke, S.; Schneemann, A.; Wutscher, A.; Fischer, R. A., Directing the Breathing Behavior of Pillared-Layered Metal Organic Frameworks via a Systematic Library of Functionalized Linkers Bearing Flexible Substituents. *J. Am. Chem. Soc.* **2012,** *134* (22), 9464-9474.

77. Matsuda, R.; Kitaura, R.; Kitagawa, S.; Kubota, Y.; Belosludov, R. V.; Kobayashi, T. C.; Sakamoto, H.; Chiba, T.; Takata, M.; Kawazoe, Y.; Mita, Y., Highly controlled acetylene accommodation in a metal-organic microporous material. *Nature* **2005,** *436* (7048), 238-241.

78. Guillerm, V.; Kim, D.; Eubank, J. F.; Luebke, R.; Liu, X.; Adil, K.; Lah, M. S.; Eddaoudi, M., A supermolecular building approach for the design and construction of metal-organic frameworks. *Chem Soc Rev* **2014,** *43* (16), 6141-72.

79. Kitaura, R.; Fujimoto, K.; Noro, S.; Kondo, M.; Kitagawa, S., A pillared-layer coordination polymer network displaying hysteretic sorption: Cu-2(pzdc)(2)(dpyg) (n) (pzdc = pyrazine-2,3-dicarboxylate; dpyg=1,2-di(4-pyridyl)glycol). *Angew. Chem. Int. Ed.* **2002,** *41* (1), 133-135.

80. Matsuda, R.; Kitaura, R.; Kitagawa, S.; Kubota, Y.; Kobayashi, T. C.; Horike, S.; Takata, M., Guest shape-responsive fitting of porous coordination polymer with shrinkable framework. *J. Am. Chem. Soc.* **2004,** *126* (43), 14063-14070.

81. Kubota, Y.; Takata, M.; Matsuda, R.; Kitaura, R.; Kitagawa, S.; Kato, K.; Sakata, M.; Kobayashi, T. C., Direct observation of hydrogen molecules adsorbed onto a microporous coordination polymer. *Angew. Chem. Int. Ed.* **2005,** *44* (6), 920-923.

82. Kitaura, R.; Kitagawa, S.; Kubota, Y.; Kobayashi, T. C.; Kindo, K.; Mita, Y.; Matsuo, A.; Kobayashi, M.; Chang, H. C.; Ozawa, T. C.; Suzuki, M.; Sakata, M.; Takata, M., Formation of a one-dimensional array of oxygen in a microporous metal-organic solid. *Science* **2002,** *298* (5602), 2358-2361.

83. Uemura, T.; Hoshino, Y.; Kitagawa, S.; Yoshida, K.; Isoda, S., Effect of organic polymer additive on crystallization of porous coordination polymer. *Chem. Mater.* **2006,** *18* (4), 992-995.

84. Tsuruoka, T.; Furukawa, S.; Takashima, Y.; Yoshida, K.; Isoda, S.; Kitagawa, S., Nanoporous nanorods fabricated by coordination modulation and oriented attachment growth.

Angew. Chem. Int. Ed. **2009,** *48* (26), 4739-43.

85. Aoki, N.; Fukuda, T.; Maeda, N.; Mae, K., Design of confluence and bend geometry for rapid mixing in microchannels. *Chem. Eng. J.* **2013,** *227*, 198-202.

86. Yamamoto, D.; Maki, T.; Watanabe, S.; Tanaka, H.; Miyahara, M. T.; Mae, K., Synthesis and adsorption properties of ZIF-8 nanoparticles using a micromixer. *Chem. Eng. J.* **2013,** *227*, 145-150.

87. Farges, F. B., Gordon E., Jr.; Rehr, J. J., Ti K-edge XANES studies of Ti coordination and disorder in oxide compounds: Comparison between theory and experiment. *Phys. Rev. B* **1997,** *56* (4), 1809-1819.

88. Shimizu, K.-i.; Maeshima, H.; Yoshida, H.; Satsuma, A.; Hattori, T., Ligand field effect on the chemical shift in XANES spectra of Cu(II) compounds. *Phys. Chem. Chem. Phys.* **2001,** *3* (5), 862-866.

89. Robert K. Szilagyi, B. S. L., Thorsten Glaser, Richard H. Holm,; Britt Hedman, K. O. H., and Edward I. Solomon, Description of the Ground State Wave Functions of Ni Dithiolenes Using Sulfur K-edge X-ray Absorption Spectroscopy. *J. Am. Chem. Soc.* **2003,** *125*, 9158-9169.

90. Mangione, G.; Sambi, M.; Nardi, M. V.; Casarin, M., A theoretical study of the L3 pre-edge XAS in Cu(II) complexes. *Phys Chem Chem Phys* **2014,** *16* (37), 19852-5.

91. Mao, L.; Rettig, S. J.; Thompson, R. C.; Trotter, J.; Xia, S. H., 2,3-Pyrazinedicarboxylates of cobalt(II), nickel(II), and copper(II); Magnetic properties and crystal structures. *Can. J. Chem.* **1996,** *74* (3), 433-444.

92. Newville, B. R. a. M., ATHENA, ARTEMIS, HEPHAESTUS: data analysis for X-ray absorption spectroscopy using IFEFFIT. *J. Synchrotron Rad.* **2005,** *12*, 537-541.

Chapter 3: Summary and outlook

The development of new multicomponent MOFs is required to expand the structural diversity. However, the search for reaction conditions is challenging and time-consuming. Therefore, understanding the mechanism of the crystallization process will be helpful in the efficient search for reaction conditions. Although the mechanism of crystal formation of MOFs has been studied so far, most of the studies are on the crystal formation process and less on the nucleation process in the early stage of the reaction, because of the evaluation of the solid state. There are few studies on the nucleation process in the early stage of the reaction, although there are many studies on the crystal growth process due to the development of evaluation methods for the solid state. In addition, no studies have focused on the individual mechanisms of multiple ligands in multicomponent MOFs. Therefore, a system to evaluate the reaction of multicomponent MOFs from multiple perspectives is needed. Micro flow reactors have been used in various fields in recent years owing to their high thermal efficiency, precise control of the mixing process, and ease of handling small amounts of solutions. Moreover, they are widely used in MOF research for the synthesis of high-quality and efficient MOFs, morphology control, and selective isolation of kinetic products.

Chapter 2 describes the crystallization mechanism of CPL-1, a typical multicomponent MOF, using a microflow reactor. The high mixing efficiency of the reactor and the correspondence between reaction time and tube distance are of great help in elucidating the mechanism of crystallization, especially in the nucleation process. A variety of channel syntheses have revealed the role of different ligands, with the pillar ligand suppressing nucleation and the layer ligand promoting it. The intermediate i_{poly}-CPL-1 in the solid state was successfully isolated from synthesis experiments with different reaction times. Immediately after the start of the reaction, i_{sol}-CPL-1/2 was formed in the supersaturated solution, and i_{poly}-CPL-1/2 in the solid state precipitated with time. Afterwards, the solid state i_{poly}-CPL-1/2 precipitates, and then changes to CPL-1/2. The stability of isol-CPL-1/2 may change depending on the mixing order of the ligands. When the pillar ligand is mixed first, the stability increases, whereas if when the layered ligand is mixed first, the stability decreases. As a result, differences in particle size were observed.

These results provide new insights into the mechanism of the crystal formation process of multicomponent MOFs. The results also help to control the particle size, which affects the properties of MOFs in the synthesis of pillared-layer MOFs. This is also a new study that shows the usefulness of a microflow channel. Previous studies on microfluidic MOFs have been successful in obtaining kinetic intermediates with the same crystal structure but with different morphologies and many defects. However, this is the first study to successfully

obtain intermediates with a different crystal structure than the final product. Although the kinetic products are difficult to isolate, in some cases, they have shown higher adsorption properties than thermodynamic products. Therefore, the use of a useful channel for the selective isolation of kinetic products could contribute to the development of superior materials.

Publication List

1. Yoko Tanaka, Yu Kitamura, Ryuji Kawano, Kan Shoji, Moe Hiratani, Tetsuo Honma, Hikaru Takaya, Hirofumi Yoshikawa, Takaaki Tsuruoka, and Daisuke Tanaka, Competing Roles of Two Kinds of Ligand during Nonclassical Crystallization of Pillared-Layer Metal-Organic Frameworks Elucidated Using Microfluidic Systems, *Chem. Eur. J.* **2020,** 26, 8889-8896

2. Yoko Tanaka, Saki Yamada and Daisuke Tanaka, Continuous fluidic Techniques for Precise Synthesis of Metal-Organic Frameworks, *ChemPlusChem*, **submitted**

Acknowledgements

The study described in this thesis has been conducted under the direction of Associate Professor Daisuke Tanaka during April, 2015 to March, 2021 at Department of Chemistry, School of Science and Technology of Kwanse Gakuin University. It would not have been possible to complete this study without the support and guidance of many people.

First and foremost, I would like to thank my supervisor, Associate Professor Daisuke Tanaka for his instructions, guidance, and constant encouragement in good and bad times throughout this work. He offered me many opportunities to visit domestic and international conferences, workshops, and collaborating laboratories, where I met many people and learned new things. I especially remember the difficulties we faced during the XAFS measurements at SPring-8. His insight and attitude toward research influenced me. I will cherish the time as we talked about many other things than just research.

I express sincere acknowledgement to co-authors, without whom none of this work would have been possible. I wish to thank Dr. Hirofumi Yoshikawa for various measurements in his lab, helpful suggestions and discussions. I would like to thank Dr. Ryuji Kawano, Dr. Shoji Kan, and Ms. Moe Hiratani for fablicating the microflow reactors. I would also like to thank Dr. Tetsuo Honma for synchrotron X-ray absorption measurements of the BL14B2 beamline in SPring-8. I wish to thank Dr. Hikaru Takaya for his guidance on the basics of XAFS measurements at the very beginning of this work and his advice on the XAFS analysis. I wish to thank Dr. Takaaki Tsuruoka for the SEM measurements and discussion of the crystallization mechanism. Throughout my research, I appreciate the opportunity of having worked with these great scientists.

Special thanks to all of the laboratory members, past and present, for their friendship and creating a pleasant atmosphere. Especially, I am deeply grateful to Ms. Yu Kitamura and Ms. Saki Yamada for discussions and feedback on the paper as co-author. I would like to thank Mr. Keito Okada and Ms. Miyako Kiyono, Mr. Yu Tsukamoto, Mr. Shota Matsuoka, and Ms. Ayumi Hirano for working with me. I would like to express my gratitude to Mr. Takuma Wakiya and Mr. Ryo Hamano, Mr. Hiroki Toshima, Mr. Keisuke Nakao, the rest of the members for discussing the research and cheering me up with the chitchat. I hope that they enjoy their research and find their own way. In addition, I started my research six years ago with Mr. Yoshinobu Kamakura and Mr. Akira Hinokimoto, Ms. Nao Shiojiri in the laboratory with nothing and only five people. I am grateful to them for having a lot of experience with them and sharing their various knowledge.

I would like to express my gratitude to all of the professors in the department of the chemistry. Thanks to their teachings, I have gained a systematic knowledge of chemistry that

formed the foundation of my research career. It was a pleasing experience to be in a favorable environment with chemists those I respect. Especially, the late Professor Hidetoshi Yamada took care of me since I was a first-year undergraduate student. Without his support, I would have left school in tears a long time back.

My parents, grandparents, and younger sisters have encouraged and provided me financial support. Without their support, I would not have been able to continue learning. I am grateful to them for receiving the blissful environment that allowed me to go to school for a long period of time.

Finally, my sincere thanks to Dr. Ryo Inoue, who provided financial support and guided me gently and strictly as a life-mentor, a researcher, and a partner. I appreciate his and Haru's support and encouragement that made the days better by my side.

December, 2020

Yoko Tanaka